



Peer review status:

This is a non-peer-reviewed preprint submitted to EarthArXiv.

# 1 **Magnetotelluric source amplitude effect**

2 **Xiaoli WAN<sup>1,2\*</sup>, Hisayoshi SHIMIZU<sup>2</sup>, Peng YU<sup>1\*</sup>, and Hisashi UTADA<sup>2,1</sup>**

3 <sup>1</sup>School of Ocean and Earth Science, Tongji University, Shanghai, China.

4 <sup>2</sup>Earthquake Research Institute, the University of Tokyo, Tokyo, Japan.

5 Corresponding authors: Xiaoli WAN (xiaolii.wan@gmail.com) and Peng YU  
6 (yupeng@tongji.edu.cn)

## 7 **Key Points:**

- 8 • The MT impedance composed of six elements is independent of the source and is a  
9 unique response function of the spherical Earth.
- 10 • 4-element spherical impedances and tippers are dependent on the source amplitude.
- 11 • 4-element and 6-element spherical impedances can be related through tippers.

## 12 **Abstract**

13 The magnetotelluric (MT) impedances of the three-dimensional (3-D) Earth are typically  
14 modelled in a Cartesian coordinate system, ignoring the curvature of the Earth's surface. This  
15 approximation is proven to be valid only for the one-dimensional (1-D) Earth. In case of the 3-D  
16 Earth, the accuracy of MT impedance estimates derived from Cartesian modeling (Cartesian  
17 impedance) must be verified by comparison with estimates obtained reliably using a spherical  
18 coordinate system (spherical impedance). While Cartesian impedances under the plane-wave  
19 approximation are known to be independent of the source, the influence of the source on  
20 spherical impedances remains poorly understood. Therefore, we conducted a systematic study of  
21 the source effects on spherical impedances through 3-D modeling for both oceanic and  
22 continental regions, employing degree-one sources. Our observations revealed that the source  
23 amplitude influences the 4-element spherical impedances and tippers. The 4-element spherical  
24 impedance is non-unique, varying with the source amplitude. Tippers are even more significantly  
25 and unavoidably affected. To address the non-uniqueness issue of the 4-element impedance, we  
26 introduced new impedance elements that incorporate induction by the radial magnetic  
27 component, deriving a novel expression for spherical impedance comprising six elements.  
28 Numerical experiments demonstrated that the 6-element spherical impedance is uniquely  
29 determined (independent of the source amplitude) when three linearly independent sources are  
30 provided. Furthermore, we derived a relation between the 6- and 4-element impedances through  
31 tippers. The relation not only accounts for the non-uniqueness of the 4-element impedance but  
32 may also explain phenomena such as seasonal variations in the impedances.

## 33 **Plain language summary**

34 This study investigates how to accurately model Earth's properties using the magnetotelluric  
35 (MT) method, a geophysical method based on measurements of electric and magnetic fields.  
36 This method explores the Earth's electrical structure by modeling the so-called MT impedance,  
37 which defines a linear relationship between the two horizontal components of the measured

38 fields. While modeling in a Cartesian coordinate system has been shown to approximate the  
39 Earth effectively in simple one-dimensional models, its reliability becomes questionable when  
40 applied to more complex three-dimensional Earth structures. To address this limitation, we  
41 conducted a systematic numerical study using a spherical coordinate system, which better  
42 accounts for the Earth's curvature. Our results revealed that the amplitude of the source  
43 (magnetic disturbances originating in the Earth's ionosphere and magnetosphere) significantly  
44 impacts the traditional MT impedance, consisting of four elements, posing challenges in  
45 accurately determining Earth's properties. To overcome this issue, we introduced a new MT  
46 impedance model consisting of six elements, which establishes a linear relationship between two  
47 horizontal electric components and three magnetic components. Numerical experiments  
48 demonstrated that this new MT impedance is essentially independent of the source amplitude,  
49 offering the potential for improved accuracy in MT modeling and inversion.

## 50 **1 Introduction**

51 The magnetotelluric (MT) method (Cagniard, 1953) is one of the most effective natural-  
52 source electromagnetic (EM) induction techniques. It utilizes the impedance, represented as the  
53 complex ratio of horizontal electric to magnetic fields, as a response function that provides  
54 information about the Earth's electrical conductivity structure. MT data consist of time series of  
55 electric and magnetic fields recorded at an array of observation sites, either on land or the ocean  
56 floor. The MT method enables the exploration of depths ranging from the near-surface to several  
57 hundred kilometers in the upper mantle. It has been extensively applied in various geophysical  
58 investigations, including the petroleum and mineral industries (e.g., Strangway et al., 1973;  
59 Livelybrooks et al., 1996; Garcia & Jones, 2000; Jiang et al., 2022), as well as studies of crustal  
60 and deep mantle structures (e.g., Stanley et al., 1977; Rosell et al., 2011; Tada et al., 2016; Zhang  
61 et al., 2016; Matsuno et al., 2017).

62 EM induction studies can be broadly classified into two approaches based on the spatial  
63 scale of the target and the range of frequencies. The first approach is referred to as global or  
64 semiglobal induction studies, in which the Earth is treated as a spherical conductor and the  
65 fundamental equation of EM induction is solved in a spherical coordinate system (e.g., Banks,  
66 1969; Schmucker, 1999a, 1999b; Shimizu et al., 2011; Kuvshinov and Semenov, 2012; Grayver  
67 et al., 2017; Guzavina et al., 2019; Zhang et al., 2023). The second approach, known as local or  
68 regional induction studies, involves observing a relatively small area of the Earth's surface,  
69 which is typically assumed to be flat. The MT method falls under this category.

70 Srivastava (1966) and Utada (2018) demonstrated that, when the induction wavenumber  
71 dominates the source wavenumber, MT impedances in both spherical and flat Earth models are  
72 equivalent, provided the Earth's structure is one-dimensional (1-D). However, MT studies  
73 are generally conducted under the flat Earth approximation, even when the three-dimensional (3-  
74 D) structure of the Earth is considered. This approximation is deemed valid for regional- and  
75 local-scale approaches conducted at mid-low latitudes and for periods up to a few hours (e.g.,  
76 Simpson & Bahr, 2005; Chave & Jones, 2012). As a result, modeling in a Cartesian coordinate  
77 system is typically preferred in MT studies due to its simplicity and advanced development  
78 compared to spherical coordinate system modeling. Advances in computational power have  
79 further facilitated the progress in 3-D MT modeling and inversion techniques. These  
80 developments now allow MT surveys to be conducted at hundreds of sites, enabling extensive  
81 spatial coverage suitable for investigating the Earth's 3-D structure (e.g., Wannamaker et al.,

82 1984; Mackie et al., 1993, 1994; Newman & Alumbaugh, 2000; Siripunvaraporn et al., 2005;  
83 Egbert & Kelbert, 2012).

84 However, 3-D modeling in a Cartesian coordinate system requires additional  
85 considerations. A Cartesian model serves as a substitute for a spherical model to study 3-D Earth  
86 structures, ignoring the Earth's curvature. This approach necessitates the use of map projections,  
87 which inevitably result in geometric distortions (Utada 2018; Grayver et al., 2019) because no  
88 map projection can simultaneously preserve area, distance, and angle. In certain cases, the  
89 modeling domain of a regional study extends horizontally over several thousand to ten thousand  
90 kilometers to account for the influence of distant lateral conductivity contrasts, such as those due  
91 to coastlines (e.g., Baba et al., 2010). Under such conditions, 3-D MT inversion using a forward  
92 code in a Cartesian coordinate system may produce artifacts due to geometric distortions  
93 introduced by a map projection. Several recent studies have identified this issue and attempted to  
94 perform 3-D MT modeling of a laterally heterogeneous Earth using spherical models to  
95 quantitatively assess the validity of employing Cartesian models for regional MT  
96 studies (Grayver et al., 2019; Luo et al., 2019; Han et al., 2020; Han & Hu, 2023). These  
97 investigations evaluated the differences between impedances calculated in Cartesian and  
98 spherical coordinate systems. However, differences exist among these studies, including the  
99 treatment of conductivity models and the source.

100 Regarding the treatment of the models, Grayver et al. (2019), Han et al. (2020), and Han  
101 and Hu (2023) examined the impedance of continental (land) regions to evaluate their modeling  
102 results. However, considering the presence of highly conductive seawater with complex  
103 bathymetric undulations and coastlines, a stronger lateral heterogeneity effect on EM induction is  
104 expected in oceanic regions. In this study, we first focus on modeling MT impedances in an  
105 oceanic region of the Philippine Sea, where a three-year-long seafloor EM survey was conducted  
106 (e.g., Baba et al., 2010; Tada et al., 2014). For comparison, we also examine the behaviors of MT  
107 impedances in a continental region of the Qinghai-Tibet Plateau in southwestern China, where a  
108 large-scale MT array study was conducted (e.g., Yang et al., 2020).

109 Regarding the treatment of the source, Luo et al. (2019), Han et al. (2020), and Han and  
110 Hu (2023) applied a combination of two orthogonal external magnetic dipoles. These dipoles  
111 generate spatially uniform fields to represent the external magnetic fields that are tangential and  
112 oriented northward and eastward, respectively, at the intersection of the equator and central  
113 meridian. Grayver et al. (2019) applied another source combination comprising three orthogonal  
114 external magnetic dipoles to ensure the matrix for calculating impedances anywhere on the Earth  
115 remains of full rank. In their study, two of the three dipoles matched those used by Luo et al.  
116 (2019), Han et al. (2020), and Han and Hu (2023), while the third dipole represented the external  
117 magnetic field directed radially at the intersection.

118 In a Cartesian model under the plane wave approximation, any pair of linearly  
119 independent sources provide unique values of impedance elements, regardless of their amplitude  
120 and polarization (Berdichevsky and Dmitriev, 1997; Berdichevsky, 1999). Therefore, in a  
121 Cartesian coordinate system, the source effect refers to the source wavenumber effect (also  
122 known as the source dimension effect; see Appendix A), which has been the focus of most  
123 related studies in the past (e.g., Schmucker, 1987; Garcia et al., 1997). However, few studies  
124 have explored source effects on MT impedances in a spherical coordinate system. This gap in  
125 literature has motivated the present study.

126 When the plane-wave approximation is not considered, there are three kinds of source  
 127 effect in MT: harmonic degree (wave number), polarization, and amplitude effects. Although  
 128 previous studies employing spherical models have applied different source combinations, none  
 129 have systematically examined the source effect on the MT impedance (Grayver et al., 2019; Luo  
 130 et al., 2019; Han et al., 2020; Han & Hu, 2023). This represents a critical issue, as the MT  
 131 impedance under plane-wave approximation intended to function as a response dependent solely  
 132 on frequency and subsurface electrical conductivity distribution, and not on the source. In this  
 133 study, we focus on the presence or absence of a source amplitude effect in spherical impedance  
 134 estimates. More specifically, we address whether the impedances obtained from various source  
 135 combinations in a spherical model are consistent, particularly with respect to the amplitude of  
 136 each external dipole source.

## 137 2 Formulations

### 138 2.1 Basic equations and coordinate systems

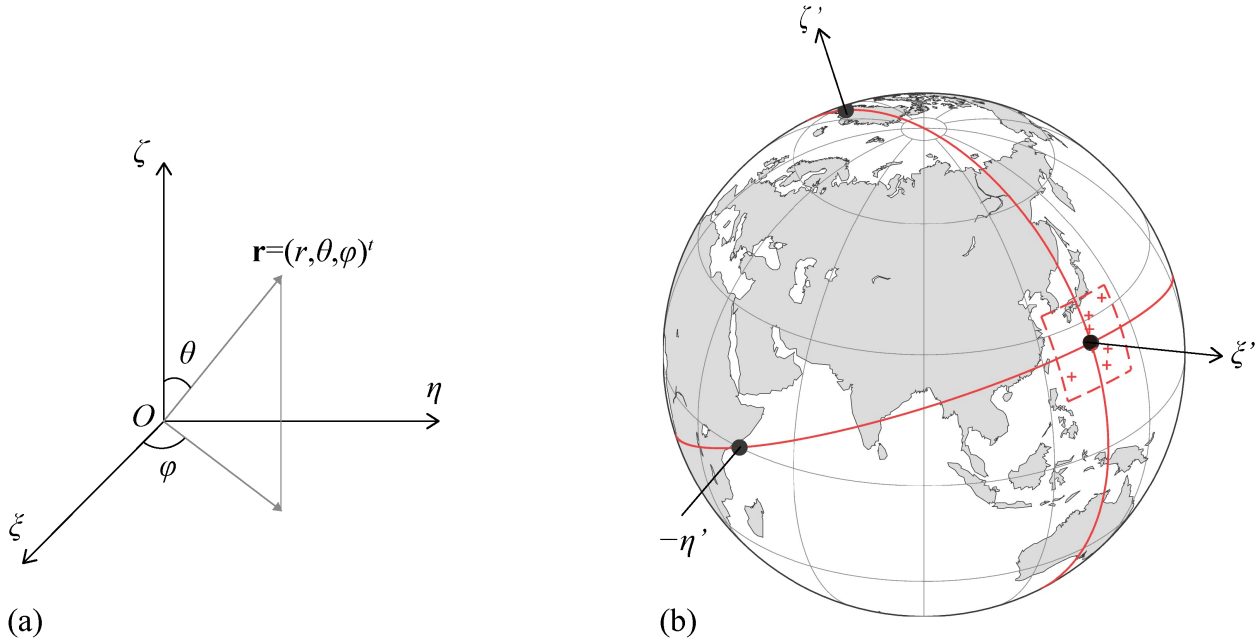
139 In this study, we perform MT forward modeling in a spherical coordinate system. We solve  
 140 the basic equations for the time-varying EM field (Maxwell's equations) in the frequency domain  
 141 as follows:

$$142 \quad \nabla \times \mathbf{E}(\mathbf{r}, \omega) = -i\omega\mu\mathbf{H}(\mathbf{r}, \omega), \quad (1)$$

$$143 \quad \nabla \times \mathbf{H}(\mathbf{r}, \omega) = \sigma(\mathbf{r})\mathbf{E}(\mathbf{r}, \omega) + \mathbf{j}^{ext}(\mathbf{r}, \omega), \quad (2)$$

144 where  $\mathbf{E}(\mathbf{r}, \omega)$  and  $\mathbf{H}(\mathbf{r}, \omega)$  denote the electric and magnetic fields at position  $\mathbf{r}$  and angular  
 145 frequency  $\omega$ . Here,  $i$  denotes the imaginary unit,  $\mu$  the magnetic permeability,  $\sigma(\mathbf{r})$  the electrical  
 146 conductivity, and  $\mathbf{j}^{ext}(\mathbf{r}, \omega)$  the source electric current density. The displacement current is  
 147 ignored in Eq. (2). We assume  $\mu = \mu_0$  everywhere, where  $\mu_0$  represents the magnetic permeability  
 148 of vacuum. We consider periods between 1,000 and 10,000 sec in modeling an oceanic region and  
 149 between 100 and 10,000 sec in modeling a continental region.

150 The position vector at any location in a geographic spherical coordinate system, with  
 151 respect to the reference coordinate system  $(\xi, \eta, \zeta)$ , is defined as  $\mathbf{r} = (r, \theta, \varphi)^t$ , where the center  
 152 of the Earth is taken as the origin (Figure 1a). Here,  $r$ ,  $\theta$ , and  $\varphi$  denote the distance from the origin,  
 153 colatitude, and longitude, respectively. Superscript  $t$  indicates the transpose.



154

(a)

(b)

155 **Figure 1.** (a) A spherical coordinate system with the center of the Earth as the origin. (b)  
 156 Coastlines on the spherical Earth. The two great circles shown as red lines represent the equator and central meridian in the rotated spherical coordinate system. Black dots mark the positions  
 157 where the  $\xi'$ ,  $\eta'$  or  $\zeta'$ - axis intersects the Earth's surface. The area enclosed by the red dashed  
 158 lines indicates the study region for the oceanic model. Red crosses denote locations of the seven  
 159 selected sites considered in later sections.  
 160

161 For numerical modeling, the longitudinal grids may become asymmetric between the  
 162 northern and southern parts of the study region if the center of the study region is not located at  
 163 the equator. Such asymmetry can lead to differences in computational precision between the  
 164 northern and southern parts of the study region (a portion of the spherical surface). To mitigate  
 165 this effect, we introduce a rotation of the reference coordinate system from  $(\xi, \eta, \zeta)$  to  $(\xi', \eta', \zeta')$   
 166 using two of the three Euler angles,  $\alpha$  and  $\beta$  (See Figure S1). The position vector with respect to  
 167 the rotated reference coordinate system  $(\xi', \eta', \zeta')$  is denoted as  $\mathbf{r}' = (r, \theta', \varphi')^t$ . In this study,  
 168 we rotate the reference coordinate system to align the intersection of the equator and central  
 169 meridian in the rotated system ( $\theta' = 90^\circ$  and  $\varphi' = 0^\circ$ ) with the center of the study region as  
 170 shown in Figure 1b.

171 It is important to note that the introduction of coordinate rotation in our study is not only  
 172 aimed at improving computational precision within a fixed coordinate system but also at  
 173 enabling a rigorous comparison between results obtained in Cartesian and spherical coordinates  
 174 at the same location with the same structural model. Moreover, when performing  
 175 electromagnetic modeling and inversion in spherical coordinates for real data applications,  
 176 achieving the highest possible computational accuracy becomes essential. Therefore,  
 177 incorporating coordinate rotation enhances both the accuracy of our current study and its  
 178 applicability to future research.

179

## 180 2.2 MT impedance and deviation

181 Using the solutions of the basic equations, we can calculate the MT impedance  $\mathbf{Z}$ , which  
 182 relates the electric and magnetic fields as follows:

$$183 \quad \mathbf{E}(\mathbf{r}_{ob}, \omega) = \mathbf{Z}(\mathbf{r}_{ob}, \omega)\mathbf{H}(\mathbf{r}_{ob}, \omega) + \delta\epsilon_{\mathbf{E}} \quad (3)$$

184 at an arbitrary observation site  $\mathbf{r}_{ob}$  and angular frequency  $\omega$ .  $\delta\epsilon_{\mathbf{E}}$  is the residual term and the  
 185 impedance is determined by solving a least squares problem to minimize  $\delta\epsilon_{\mathbf{E}}^2$ . In conventional  
 186 MT, two horizontal components of the EM fields are considered in Eq. (3); therefore, the  
 187 impedance is a complex-valued  $2 \times 2$  (4-element) tensor.

188 In this study, the location of each observation site is specified by the colatitude ( $\theta$ ) and  
 189 longitude ( $\varphi$ ) in the original spherical coordinate system. At any observation site, the directions  
 190 of tangential axes in the rotated spherical coordinate system (positive  $\theta'$  and  $\varphi'$ ) deviate from  
 191 those of positive  $\theta$  and  $\varphi$  in the original spherical coordinate system. The impedance elements  
 192 calculated by modeling in the rotated spherical coordinate system were converted to those  
 193 defined in the original spherical coordinate system to ensure consistency with actual field  
 194 measurements. The four impedance elements are denoted as  $Z_{ij}(\mathbf{r}_{ob}, \omega)$  where subscripts  $i$  and  $j$   
 195 denote  $\theta$  or  $\varphi$ . Hereafter, the position and frequency dependences of electromagnetic fields and  
 196 impedances,  $(\mathbf{r}_{ob}, \omega)$ , are omitted for simplicity.

197 To compare the impedances calculated at a location  $\mathbf{r}_{ob}$  and frequency  $\omega$  under different  
 198 conditions (source combinations, for example) 1 and 2, we use the Frobenius norm (F-norm)  
 199 deviation, defined as:

$$200 \quad dZ^{1-2} = \frac{\|\mathbf{Z}^1 - \mathbf{Z}^2\|_F}{\|\mathbf{Z}^2\|_F}, \quad (4)$$

201 where  $\mathbf{Z}^1$  and  $\mathbf{Z}^2$  are the two impedances to be compared. The F-norm of  $\mathbf{Z}$  is defined as:

$$202 \quad \|\mathbf{Z}\|_F = \{\text{tr}(\mathbf{Z}^H \mathbf{Z})\}^{1/2} = \left\{ \sum_{i,j} |Z_{ij}|^2 \right\}^{1/2}, \quad (5)$$

203 where superscript  $H$  denotes the Hermitian (complex conjugate) transpose.

204 In certain cases, we calculate the average F-norm deviation over the entire study region,  
 205 which is defined as:

$$206 \quad dZ_{avg}^{1-2} = \frac{1}{N} \sum_{n=1}^N \frac{\|\mathbf{Z}_n^1 - \mathbf{Z}_n^2\|_F}{\|\mathbf{Z}_n^2\|_F}, \quad (6)$$

207 where subscript  $n$  represents a calculation cell, and  $N$  is the total number of calculation cells in  
 208 the study region on the seafloor (oceanic model) or the surface (continental model).

209 In this study, we set the target level of the F-norm deviation of impedance to 0.01, which is a  
 210 typical error level of the MT impedance in case of seafloor observations (Tada et al., 2012). In  
 211 subsequent comparisons, two impedances are considered consistent when the F-norm deviation  
 212 is smaller than this target level.

213 To represent the complex-valued elements of the impedance, the apparent resistivity and  
 214 impedance phase are also used, defined as:

$$215 \quad \rho_{a_{ij}} = \frac{|Z_{ij}|^2}{\omega\mu_0} \quad (7)$$

216 and

$$217 \quad \phi_{ij} = \arg[Z_{ij}], \quad (8)$$

218 respectively. In several cases, we compared the spatial distributions and differences of the  
 219 numerically calculated  $\rho_{a_{ij}}$  and  $\phi_{ij}$ , along with the F-norm deviation of the impedance  $Z$ ,  
 220 between two modeling results. The differences in  $\rho_{a_{ij}}$  and  $\phi_{ij}$  are defined as:

$$221 \quad d\rho_{a_{ij}}^{1-2} = \frac{\rho_{a_{ij}}^1}{\rho_{a_{ij}}^2} \quad (9)$$

222 and

$$223 \quad d\phi_{ij}^{1-2} = \phi_{ij}^1 - \phi_{ij}^2, \quad (10)$$

224 respectively.

### 225 2.3 External source

226 In a rotated spherical coordinate system, we consider an external magnetic source of  
 227 spherical harmonic degree one (dipole term), which generates a spatially uniform field. The  
 228 external magnetic field above the Earth's surface ( $r > r_e$ , where  $r_e = 6371$  km is the Earth's  
 229 radius) can be obtained from the spatial gradient of the scalar potential, generally expressed by  
 230 the spherical harmonic expansion as:

$$231 \quad V(r, \theta', \varphi', \omega) = r(q_1^0(\omega) \cos \theta' + q_1^1(\omega) \cos \varphi' \sin \theta' + s_1^1(\omega) \sin \varphi' \sin \theta'), \quad (11)$$

232 where  $q_1^0(\omega)$ ,  $q_1^1(\omega)$ , and  $s_1^1(\omega)$  are expansion coefficients of the axial and two equatorial dipole  
 233 terms, respectively.

234 Using  $\mathbf{B} = -\nabla V$  and  $\mathbf{H} = \frac{\mathbf{B}}{\mu_0}$ , the three components of the external magnetic field are  
 235 obtained as:

$$236 \quad H_r(r, \theta', \varphi', \omega) = -\frac{1}{\mu_0}(q_1^0(\omega) \cos \theta' + q_1^1(\omega) \cos \varphi' \sin \theta' + s_1^1(\omega) \sin \varphi' \sin \theta'), \quad (12)$$

$$237 \quad H_\theta(r, \theta', \varphi', \omega) = -\frac{1}{\mu_0}(-q_1^0(\omega) \sin \theta' + q_1^1(\omega) \cos \varphi' \cos \theta' + s_1^1(\omega) \sin \varphi' \cos \theta'), \quad (13)$$

238 and

$$239 \quad H_\varphi(r, \theta', \varphi', \omega) = -\frac{1}{\mu_0}(-q_1^1(\omega) \sin \varphi' + s_1^1(\omega) \cos \varphi'). \quad (14)$$

240 For convenience, we represent the three basis sources (external dipoles) in the rotated spherical  
 241 coordinate system by three unit vectors in  $\zeta'$ ,  $\xi'$ , and  $\eta'$  directions, denoted as  $\hat{\mathbf{S}}_{\zeta'}$ ,  $\hat{\mathbf{S}}_{\xi'}$ , and  $\hat{\mathbf{S}}_{\eta'}$ ,  
 242 corresponding to the harmonic expansion coefficients  $q_1^0$ ,  $q_1^1$ , and  $s_1^1$ , respectively (Figure 2a).



243 By setting  $\frac{q_1^0(\omega)}{\mu_0} = \frac{q_1^1(\omega)}{\mu_0} = \frac{s_1^1(\omega)}{\mu_0} = -1$ , these sources generate uniform magnetic fields of unit  
 244 amplitude in the positive  $\zeta'$ -,  $\xi'$ -, and  $\eta'$ - directions, respectively. An arbitrary source in the  
 245 rotated spherical coordinate system, denoted as  $\mathbf{S}(\theta'_S, \varphi'_S)$  is specified by the pole location  
 246  $(\theta'_S, \varphi'_S)$  (Figure 2b). The source  $\mathbf{S}$  can be expressed by a linear combination of the three basis  
 247 sources:

$$248 \quad \mathbf{S}(\theta'_S, \varphi'_S) = a_{\zeta'} \hat{\mathbf{S}}_{\zeta'} + a_{\eta'} \hat{\mathbf{S}}_{\eta'} + a_{\xi'} \hat{\mathbf{S}}_{\xi'}, \quad (15)$$

249 where  $a_{\zeta'}$ ,  $a_{\eta'}$ , and  $a_{\xi'}$  are real-valued arbitrary amplitude factors. For a normalized source, the  
 250 unit amplitude expression in an arbitrary direction is given by:

$$251 \quad \hat{\mathbf{S}}(\theta'_S, \varphi'_S) = \hat{a}_{\zeta'} \hat{\mathbf{S}}_{\zeta'} + \hat{a}_{\eta'} \hat{\mathbf{S}}_{\eta'} + \hat{a}_{\xi'} \hat{\mathbf{S}}_{\xi'}, \quad (16)$$

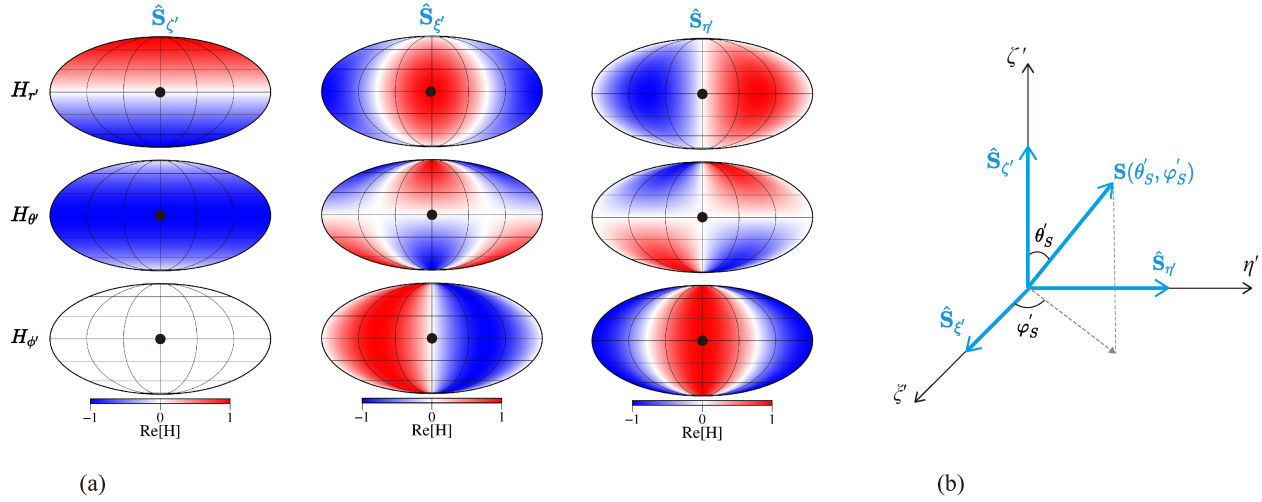
252 where

$$253 \quad \hat{a}_{\zeta'} = \frac{a_{\zeta'}}{|\mathbf{S}(\theta'_S, \varphi'_S)|} = \cos \theta'_S, \quad (17)$$

$$254 \quad \hat{a}_{\eta'} = \frac{a_{\eta'}}{|\mathbf{S}(\theta'_S, \varphi'_S)|} = \sin \theta'_S \sin \varphi'_S, \quad (18)$$

255 and

$$256 \quad \hat{a}_{\xi'} = \frac{a_{\xi'}}{|\mathbf{S}(\theta'_S, \varphi'_S)|} = \sin \theta'_S \cos \varphi'_S. \quad (19)$$



257 (a) Distribution of magnetic field components on a spherical surface for the three basis  
 258 sources in the rotated coordinate system. The black dots mark the location of the intersection of  
 259 the equator and central meridian. (b) External dipole sources in the rotated coordinate  
 260 system.  $\mathbf{S}$  is a source dipole of arbitrary polarization and amplitude with one of its poles located  
 261 at  $(\theta'_S, \varphi'_S)$ .  
 262

263 The external field generated by an arbitrary source  $\mathbf{S}$  is expressed as  $\mathbf{H}_{ext}(r, \theta', \varphi', \omega, \mathbf{S})$ .  
 264 Using Eq. (15) and the linearity of the EM field, this can be written as:

$$265 \quad \mathbf{H}_{ext}(r, \theta', \varphi', \omega, \mathbf{S}) = a_{\zeta'} \mathbf{H}_{ext}(r, \theta', \varphi', \omega, \hat{\mathbf{S}}_{\zeta'}) + a_{\eta'} \mathbf{H}_{ext}(r, \theta', \varphi', \omega, \hat{\mathbf{S}}_{\eta'}) + a_{\xi'} \mathbf{H}_{ext}(r, \theta', \varphi', \omega, \hat{\mathbf{S}}_{\xi'}), \quad (20)$$

266 where

$$267 \quad \mathbf{H}_{ext}(r, \theta', \varphi', \omega, \hat{\mathbf{S}}_{\zeta'}) = -\frac{q_1^0(\omega)}{\mu_0} \begin{pmatrix} \cos \theta' \\ -\sin \theta' \\ 0 \end{pmatrix} = \begin{pmatrix} \cos \theta' \\ -\sin \theta' \\ 0 \end{pmatrix}, \quad (21)$$

$$268 \quad \mathbf{H}_{ext}(r, \theta', \varphi', \omega, \hat{\mathbf{S}}_{\eta'}) = -\frac{q_1^1(\omega)}{\mu_0} \begin{pmatrix} \sin \theta' \cos \varphi' \\ \cos \theta' \cos \varphi' \\ -\sin \varphi' \end{pmatrix} = \begin{pmatrix} \sin \theta' \cos \varphi' \\ \cos \theta' \cos \varphi' \\ -\sin \varphi' \end{pmatrix}, \quad (22)$$

269 and

$$270 \quad \mathbf{H}_{ext}(r, \theta', \varphi', \omega, \hat{\mathbf{S}}_{\xi'}) = -\frac{s_1^1(\omega)}{\mu_0} \begin{pmatrix} \sin \theta' \sin \varphi' \\ \cos \theta' \sin \varphi' \\ \cos \varphi' \end{pmatrix} = \begin{pmatrix} \sin \theta' \sin \varphi' \\ \cos \theta' \sin \varphi' \\ \cos \varphi' \end{pmatrix}. \quad (23)$$

271 These external fields given in Eq. (21)-(23) correspond to  $-H^1$ ,  $-H^2$ , and  $-H^3$  in Grayver et al.  
272 (2019).

273 The Maxwell's equations are solved by providing a source boundary condition at the  
274 outer boundary of the model domain using Eqs. (21)–(23). The resulting solutions for the source  
275  $\hat{\mathbf{S}}_{\zeta'}$ , for example, are denoted as  $\mathbf{E}(r, \theta', \varphi', \omega, \hat{\mathbf{S}}_{\zeta'})$  and  $\mathbf{H}(r, \theta', \varphi', \omega, \hat{\mathbf{S}}_{\zeta'})$ . The solutions for an  
276 arbitrary source  $\mathbf{S}$  can then be obtained as a linear combination of the solutions for the three basis  
277 sources:

$$278 \quad \mathbf{E}(r, \theta', \varphi', \omega, \mathbf{S}) = a_{\zeta'} \mathbf{E}(r, \theta', \varphi', \omega, \hat{\mathbf{S}}_{\zeta'}) + a_{\eta'} \mathbf{E}(r, \theta', \varphi', \omega, \hat{\mathbf{S}}_{\eta'}) + a_{\xi'} \mathbf{E}(r, \theta', \varphi', \omega, \hat{\mathbf{S}}_{\xi'}) \quad (24)$$

279 and

$$280 \quad \mathbf{H}(r, \theta', \varphi', \omega, \mathbf{S}) = a_{\zeta'} \mathbf{H}(r, \theta', \varphi', \omega, \hat{\mathbf{S}}_{\zeta'}) + a_{\eta'} \mathbf{H}(r, \theta', \varphi', \omega, \hat{\mathbf{S}}_{\eta'}) + a_{\xi'} \mathbf{H}(r, \theta', \varphi', \omega, \hat{\mathbf{S}}_{\xi'}), \quad (25)$$

281 respectively.

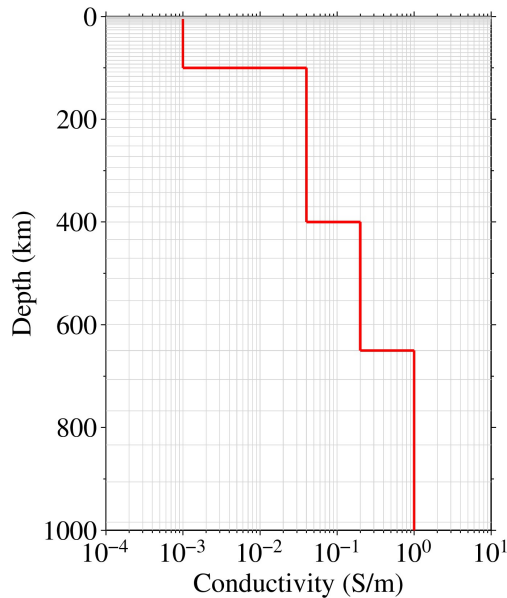
282 In this numerical modeling study, the MT impedance is estimated from the EM field  
283 solutions by providing a set of external dipole sources. A set of two or three sources is denoted  
284 by  $\{\mathbf{S}_1, \mathbf{S}_2\}$  or  $\{\mathbf{S}_1, \mathbf{S}_2, \mathbf{S}_3\}$ , respectively, where  $\mathbf{S}_1$ ,  $\mathbf{S}_2$ , and  $\mathbf{S}_3$  are external dipole sources with  
285 arbitrary directions and amplitudes.

### 286 **3 Model setup**

#### 287 **3.1 Modeling methods and surface inhomogeneities**

288 Modeling in a spherical coordinate system was performed using a global forward code  
289 modified from Uyeshima and Schultz (2000). This code employs a staggered-grid finite  
290 difference method to solve Maxwell's equations, with all variables calculated in double  
291 precision. The source field, as expressed in Eq. (20), was set at the outer boundary of the model  
292 domain ( $r = 10r_e$ ). The source altitude was chosen sufficiently far from the Earth's surface to  
293 ensure that the internal part of the primary field is negligible. The inner boundary was set at the  
294 core-mantle boundary (CMB) ( $r = 3479$  km), where the radial magnetic field component is set  
295 to zero as a boundary condition. Convergence of the numerical solution was confirmed through  
296 iteration, when the normalized change in the magnetic field solution, defined by the dot products  
297 of the magnetic vector integrated over the entire calculation domain, reached  $10^{-16}$ .

298 The model assumes the Earth's interior to consist of two thin, laterally heterogeneous  
 299 shells on the surface and a 1-D (radially symmetric) structure beneath them. The shallowest layer  
 300 is a 4-km-thick inhomogeneous shell representing the land-sea electrical conductivity contrast,  
 301 with variable conductance reflecting bathymetric undulations. Land topography is ignored  
 302 because conductance is smaller on land than in the sea. The second layer is a 1-km-thick  
 303 inhomogeneous shell that simulating lateral variations in oceanic sediment thickness. Figure 3  
 304 shows the assumed 1-D profile below these two shells, which was designed with reference to the  
 305 oceanic mantle model of the western Pacific (Baba et al., 2010; Shimizu et al., 2010), with  
 306 simplifications.



307  
 308 **Figure 3.** 1-D electrical conductivity structure and the radial gridding (depth from 5 km to 1,000  
 309 km) assumed for the numerical models. The structure is designed by considering the 1-D  
 310 structures beneath the Pacific obtained by Baba et al. (2010) and Shimizu et al. (2010).

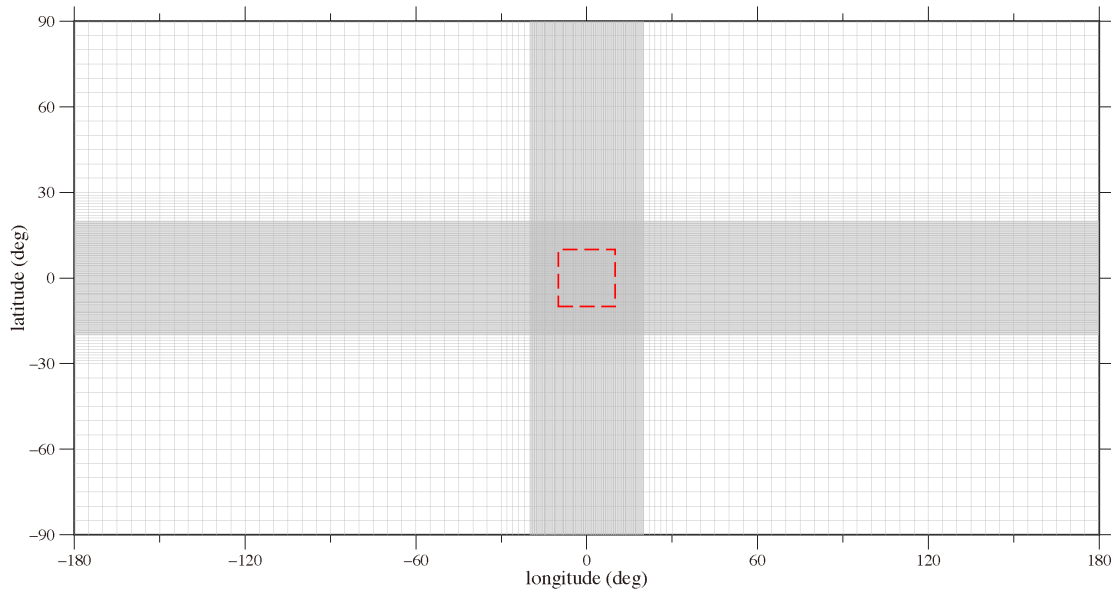
311 We assumed electrical conductivities of the sea water, sediment, and crustal rock in the  
 312 two surface shells to be 3.0, 0.1, and 0.01 S/m, respectively. For the oceanic area of the surface  
 313 shell, we first averaged the bathymetry data from ETOPO1 (Amante & Eakins, 2009), which  
 314 originally had a resolution of  $1' \times 1'$ , within each cell. The conductance and average conductivity  
 315 in the 4 km-thick surface shell were calculated under the assumption of homogeneous  
 316 conductivity within each cell. For the sediment shell, we employed the Laske and Masters (1997)  
 317 model. The sediment thickness, originally provided at a resolution of  $1^\circ \times 1^\circ$ , was first  
 318 interpolated, and then the conductance and average conductivity were calculated in a manner  
 319 similar to that used for the first shell. In the oceanic model, the MT impedance was estimated at  
 320 the seafloor (the boundary between the top two heterogeneous shells) using the modeled EM  
 321 solutions. In the continental model, the MT impedance was estimated at the surface.

### 322 3.2 Grid spacing

323 We adopted identical grid spacings for both the oceanic and continental models to  
 324 facilitate comparison. Because it is not practical to solve the basic equations with a fine grid  
 325 spacing across the entire modeling domain, non-uniform gridding is applied in both the radial  
 326 and tangential directions. The lateral size of the study region was defined as  $20^\circ \times 20^\circ$ . The

327 center of the study region was set at (25°N, 135°E) for the oceanic model and at (32°N, 90° E)  
 328 for the continental model. These center locations were then positioned at (0°N, 0°E) in the  
 329 rotated coordinate system.

330 The radial grid spacing was uniformly set to 500 m in the land-sea contrast shell and to  
 331 250 m in the sediment shell. In the 1-D shells, the radial grid spacing gradually increased  
 332 following logarithmic equidistance (Fujita et al., 2018) until the CMB. The lateral grid size was  
 333 set to 0.25° in the central area, including the study region, and gradually widened to 1°, 2°, and  
 334 5°, depending on the distance from the center. The area of the finest (0.25°) grids was defined as  
 335 40° × 40° based on numerical tests (Figure 4, S2, and Table S1 for the influence of the area of  
 336 the finest grids). The radial grid spacing near the seafloor was confirmed to be sufficiently fine  
 337 for the 3-D model (Figure S3). In total, the grid system consisted of 89 cells in the  $r$ -direction,  
 338 including 17 cells in the air, 194 cells in the  $\theta'$ -direction, and 230 cells in the  $\varphi'$ -direction.



339  
 340 **Figure 4.** Lateral grid spacing for spherical model in the rotated coordinate system. The red  
 341 dashed square indicates the study region.

#### 342 **4 Influence of the source on estimating the MT impedance in a spherical model**

343 To obtain four elements of the MT impedance from the EM components of numerical  
 344 modeling solutions, at least two linearly independent sources are required. In the case of a  
 345 Cartesian model under the plane-wave approximation, the MT impedance is known to be  
 346 independent of the source amplitude and polarization, and therefore serves as an EM response  
 347 function of the Earth (See Appendix B). In a spherical model, the conventional impedance,  
 348 consisting of four elements, can be estimated from the EM solutions for two independent sources  
 349 by solving (Grayver et al., 2019)

$$350 \begin{pmatrix} E_{\theta}^1 & E_{\theta}^2 \\ E_{\varphi}^1 & E_{\varphi}^2 \end{pmatrix} = \begin{pmatrix} Z_{\theta\theta} & Z_{\theta\varphi} \\ Z_{\varphi\theta} & Z_{\varphi\varphi} \end{pmatrix} \begin{pmatrix} H_{\theta}^1 & H_{\theta}^2 \\ H_{\varphi}^1 & H_{\varphi}^2 \end{pmatrix}, \quad (26)$$

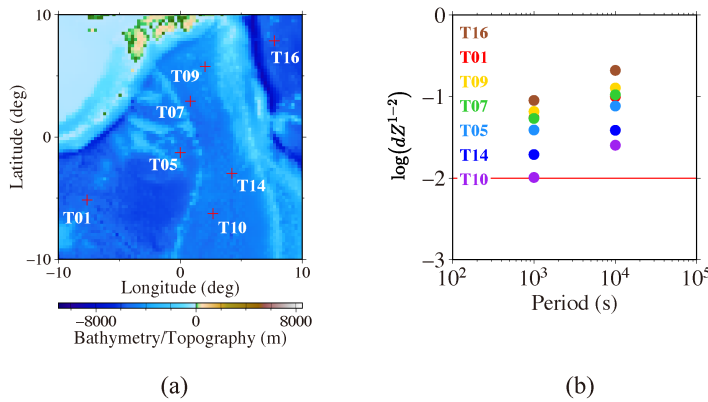
351 where superscripts 1 and 2 denote two linearly independent external sources.

352 By re-writing Eq. (26), we obtain a positive definite system of equations  $\mathbf{b} = \mathbf{A}\mathbf{x}$ , where  
 353  $\mathbf{b}$  is a vector composed of modelled electric field components  $E_{\theta}^1, E_{\theta}^2, E_{\varphi}^1$ , and  $E_{\varphi}^2$ ,  $\mathbf{A}$  is a matrix  
 354 composed of modelled magnetic components  $H_{\theta}^1, H_{\theta}^2, H_{\varphi}^1$ , and  $H_{\varphi}^2$ , and  $\mathbf{x}$  is a vector composed of  
 355 four impedance elements  $Z_{\theta\theta}, Z_{\theta\varphi}, Z_{\varphi\theta}$ , and  $Z_{\varphi\varphi}$ . The unknown vector  $\mathbf{x}$  can be obtained by

$$356 \quad \mathbf{x} = (\mathbf{A}^H \mathbf{A})^{-1} \mathbf{A}^H \mathbf{b}. \quad (27)$$

357 Grayver et al. (2019) pointed out that solving Eq. (27) is not globally feasible because matrix  $\mathbf{A}$   
 358 may not be of full rank at the pole location of the source dipole field. However, it is possible to  
 359 estimate four elements of the impedance using two independent sources within a specific part of  
 360 the Earth's surface (the study region), where the matrix rank is confirmed to be full.

361 Here, we considered the oceanic model (Figure 5a), which includes the study region of a  
 362 seafloor MT experiment conducted in the Philippine Sea by Baba et al. (2010). We calculated the  
 363 MT impedances in the rotated spherical coordinate system for two periods: 1,000 and 10,000 sec.  
 364 We compared two results obtained by using different combinations of external dipole sources of  
 365 unit intensity:  $\{\hat{\mathbf{S}}_{\zeta'}, \hat{\mathbf{S}}_{\eta'}\}$  and  $\{\hat{\mathbf{S}}(45^\circ, 45^\circ), \hat{\mathbf{S}}(135^\circ, 45^\circ)\}$ . The first source combination provides  
 366 the best similarity to MT modeling in a Cartesian coordinate system with two orthogonal plane-  
 367 wave sources polarized in the N-S and E-W directions. These two combinations are chosen for  
 368 this experiment because they exhibit the largest angular distance from each other. The results at  
 369 seven selected sites showed significant F-norm deviations (Figure 5b), indicating that the  
 370 impedance estimated using these two sources is non-unique but depends on the source  
 371 polarization. Through further systematic numerical experiments, we confirmed that in a spherical  
 372 coordinate system, impedances obtained from an arbitrary pair of orthogonal sources are unique  
 373 only when the sources lie within a single great circle plane and have no components normal to  
 374 that plane.



375 (a) (b)

376 **Figure 5.** (a) A map showing the bathymetry and site locations of the oceanic model. Red  
 377 crosses show the seven selected sites (after Baba et al., 2010). (b) F-norm deviations at seven  
 378 selected sites between calculated impedances with source combinations of  $\{\hat{\mathbf{S}}(45^\circ, 45^\circ), \hat{\mathbf{S}}(135^\circ,$   
 379  $45^\circ)\}$  and  $\{\hat{\mathbf{S}}_{\zeta'}, \hat{\mathbf{S}}_{\eta'}\}$ . Model: the oceanic model in a rotated spherical coordinate system.

380 Next, we consider three independent sources to estimate the impedance, as suggested by  
 381 Grayver et al. (2019), to address the problem of non-uniqueness in impedance determination. We  
 382 attempted to estimate the four elements of the MT impedance from the modeling results with  
 383 three orthogonal sources of unit amplitude by solving the matrix equation of an overdetermined  
 384 system:

$$\begin{pmatrix} E_{\theta}^1 & E_{\theta}^2 & E_{\theta}^3 \\ E_{\varphi}^1 & E_{\varphi}^2 & E_{\varphi}^3 \end{pmatrix} = \begin{pmatrix} Z_{\theta\theta} & Z_{\theta\varphi} \\ Z_{\varphi\theta} & Z_{\varphi\varphi} \end{pmatrix} \begin{pmatrix} H_{\theta}^1 & H_{\theta}^2 & H_{\theta}^3 \\ H_{\varphi}^1 & H_{\varphi}^2 & H_{\varphi}^3 \end{pmatrix} + \begin{pmatrix} \delta\epsilon_{E_{\theta}}^1 & \delta\epsilon_{E_{\theta}}^2 & \delta\epsilon_{E_{\theta}}^3 \\ \delta\epsilon_{E_{\varphi}}^1 & \delta\epsilon_{E_{\varphi}}^2 & \delta\epsilon_{E_{\varphi}}^3 \end{pmatrix}, \quad (28)$$

386 where superscripts 1, 2, and 3 represent the EM solutions for the respective independent sources.  
 387 Rewriting Eq. (28), we obtain an overdetermined system of linear equations  $\mathbf{b} = \mathbf{A}\mathbf{x} + \delta\epsilon_{\mathbf{E}}$ ,  
 388 which can be solved by minimizing the residual term, as in the case of Eq. (27).

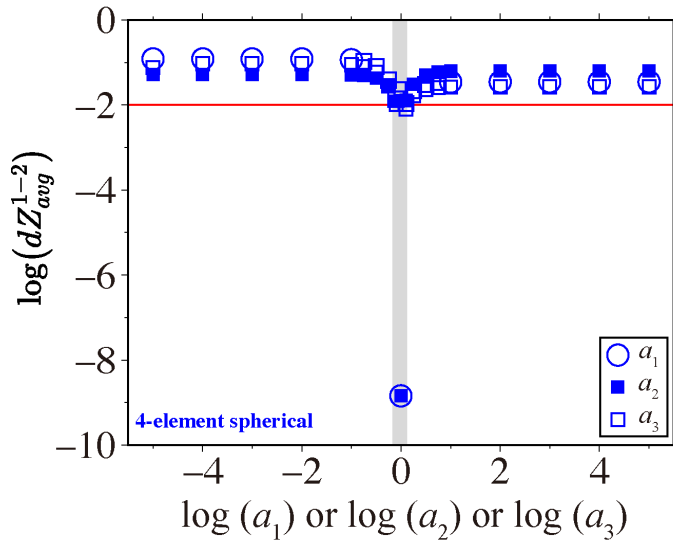
389 Similar to the previous experiment, the modelled impedances were examined and  
 390 compared using two different source combinations in the oceanic model. In each source  
 391 combination, two sources were kept to be the same as in the previous case, and a third source  
 392 orthogonal to the other two was added. The source combinations considered are  $\{\hat{\mathbf{S}}_{\zeta'}, \hat{\mathbf{S}}_{\eta'}, \hat{\mathbf{S}}_{\xi'}\}$   
 393 and  $\{\hat{\mathbf{S}}(45^\circ, 45^\circ), \hat{\mathbf{S}}(135^\circ, 45^\circ), \hat{\mathbf{S}}(90^\circ, 135^\circ)\}$ . The newly added basis source,  $\hat{\mathbf{S}}_{\xi'}$ , produces a  
 394 magnetic field only in the radial direction at the center of the study region in the rotated spherical  
 395 coordinate system.

396 For both source combinations, the four elements of the MT impedance were estimated  
 397 using Eq. (28). The F-norm deviations at all selected sites turned out very small, at the level of  
 398  $10^{-9}$ , indicating that the impedances estimated from the two source combinations were consistent.  
 399 Differences in the apparent resistivities and impedance phases were also sufficiently small, at a  
 400 level of  $10^{-9}$ – $10^{-8}$  (See Figure S5).

401 The source combinations described above, which provide unique impedances, consist of  
 402 three mutually orthogonal external dipole sources with equal (unit) amplitudes. However, natural  
 403 source fields (geomagnetic disturbances) are complex; their amplitudes and polarizations change  
 404 dynamically over time. To examine whether more complex source combinations with different  
 405 polarizations and amplitudes yield unique impedances as shown above, we conducted further  
 406 numerical experiments and compared the impedances estimated from various source  
 407 combinations. When one of the three sources is not orthogonal to the other two, it can be  
 408 decomposed into three sources so that one of them is orthogonal to the other two, thereby  
 409 independently contributing to impedance estimation. Thus, the source polarization effect can  
 410 essentially be regarded as a source amplitude effect. We considered cases in which two of the  
 411 three orthogonal sources had unit amplitudes, while the amplitude of the third source was varied.

412 The source combinations examined were:  $\{a_1\hat{\mathbf{S}}(45^\circ, 45^\circ), \hat{\mathbf{S}}(135^\circ, 45^\circ), \hat{\mathbf{S}}(90^\circ, 135^\circ)\}$ ,  
 413  $\{\hat{\mathbf{S}}(45^\circ, 45^\circ), a_2\hat{\mathbf{S}}(135^\circ, 45^\circ), \hat{\mathbf{S}}(90^\circ, 135^\circ)\}$  and  $\{\hat{\mathbf{S}}(45^\circ, 45^\circ), \hat{\mathbf{S}}(135^\circ, 45^\circ), a_3\hat{\mathbf{S}}(90^\circ, 135^\circ)\}$   
 414 where amplitude factor,  $a_1$ ,  $a_2$ , and  $a_3$  took values  $10^{-0.5}$ , 1, and  $10^{0.5}$ , respectively. The  
 415 impedances calculated from these source combinations in the oceanic model were compared with  
 416 those obtained from the reference source combination  $\{\hat{\mathbf{S}}_{\zeta'}, \hat{\mathbf{S}}_{\eta'}, \hat{\mathbf{S}}_{\xi'}\}$ . The F-norm deviations of  
 417 the impedance obtained at seven selected sites exceeded 0.01 at most sites when  $a_1$ ,  $a_2$ , or  $a_3$   
 418 was  $10^{-0.5}$  or  $10^{0.5}$  (See Figure S6). Additionally, the largest deviation occurred at T16 or T09,  
 419 while the smallest deviation was observed at T10, suggesting that the deviation decreases with  
 420 increasing distance from the coastlines and/or the areas with steep bathymetric changes.  
 421 Differences in the apparent resistivity and impedance phase also showed significant anomalies  
 422 not only near coastlines but also in flat basins (see Figure S7 for the case where  $a_1$  is  $10^{-0.5}$ ).  
 423 These results suggest that the impedance estimated from the three independent sources depends  
 424 on the source amplitude.

425 Next, the average F-norm deviation of the impedance was calculated for the entire study  
 426 region over a wider range of amplitude factors. The impedances obtained from different values  
 427 of  $a_1$ ,  $a_2$ , and  $a_3$  were compared with those from the reference source combination consisting of  
 428 three basis sources. The amplitude factors  $a_1$  (represented by open blue circles),  $a_2$  (represented  
 429 by solid blue squares), and  $a_3$  (represented by open blue squares) varied between  $10^{-5}$  and  $10^5$ .  
 430 The results are shown in Figure 6. We found that the averaged deviations were approximately  $10^{-9}$   
 431 only when  $a_1$ ,  $a_2$ , and  $a_3$  were exactly 1. Outside this narrow range near unity, the F-norm  
 432 deviations exceeded the typical observation error level (0.01), with the largest deviation at a level  
 433 of 0.1. The deviations also exhibited slight asymmetry with respect to the unit amplitudes. The  
 434 results of these numerical experiments clearly indicate that the MT impedance consisting of four  
 435 elements is not unique and depends on the source amplitude.



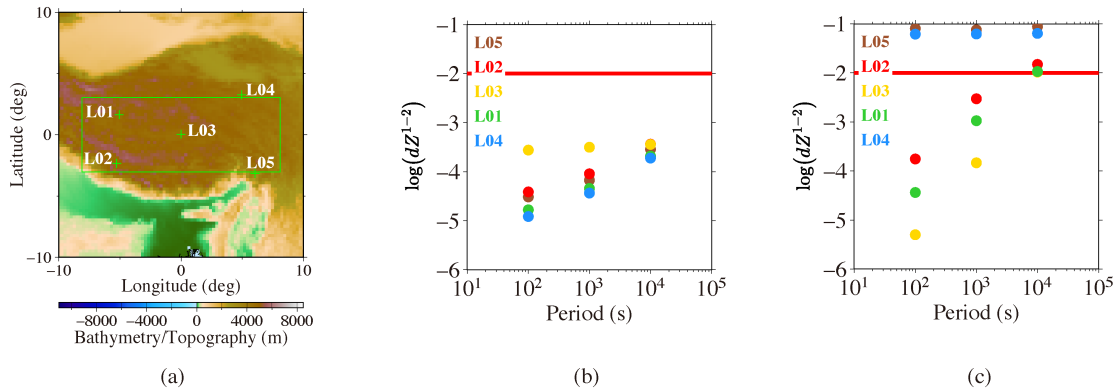
436

437 **Figure 6.** Dependence of  $dZ_{avg}^{1-2}$  on  $\log(a_1)$ ,  $\log(a_2)$ , or  $\log(a_3)$  in a range when  $a_1$ ,  $a_2$  or  $a_3$  is  
 438 between  $10^{-5}$  and  $10^5$  in the entire study region at period of 10,000 sec. Open blue circles  
 439 represent  $dZ_{avg}^{1-2}$  between the 4-element impedances from source combination of  $\{a_1 \hat{\mathbf{S}}(45^\circ, 45^\circ),$   
 440  $\hat{\mathbf{S}}(135^\circ, 45^\circ), \hat{\mathbf{S}}(90^\circ, 135^\circ)\}$  and from  $\{\hat{\mathbf{S}}_{\zeta'}, \hat{\mathbf{S}}_{\eta'}, \hat{\mathbf{S}}_{\xi'}\}$ , solid blue squares between those from  
 441 source combination of  $\{\hat{\mathbf{S}}(45^\circ, 45^\circ), a_2 \hat{\mathbf{S}}(135^\circ, 45^\circ), \hat{\mathbf{S}}(90^\circ, 135^\circ)\}$  and from  $\{\hat{\mathbf{S}}_{\zeta'}, \hat{\mathbf{S}}_{\eta'}, \hat{\mathbf{S}}_{\xi'}\}$ ,  
 442 and open blue squares between those from  $\{\hat{\mathbf{S}}(45^\circ, 45^\circ), \hat{\mathbf{S}}(135^\circ, 45^\circ), a_3 \hat{\mathbf{S}}(90^\circ, 135^\circ)\}$ , and  
 443  $\{\hat{\mathbf{S}}_{\zeta'}, \hat{\mathbf{S}}_{\eta'}, \hat{\mathbf{S}}_{\xi'}\}$ . Hatched area corresponds to horizontal range of  $a_i$  considered in Section 6.  
 444 Model: the oceanic model in a rotated spherical coordinate system.

445 We conducted an additional experiment on the continental model of the Qinghai-Tibet  
 446 Plateau region (Figure 7a). Two tests were performed: one with and one without a highly  
 447 conductive anomaly (Yang et al., 2020). In the model with the anomaly, a polygonal structure  
 448 with a conductivity of 0.1 S/m was assumed, centered in the study region and to have dimensions  
 449 of  $16^\circ \times 6^\circ$  laterally (represented by the green rectangle in Figure 7a), extending from 4 to 100  
 450 km in depth. In the absence of the 3-D anomaly, the model is nearly 1-D because the study  
 451 region is far from the coastlines and the crust and mantle are assumed to be laterally  
 452 homogeneous with a conductivity of 100 S/m.

453 We first examined the case without a 3-D anomaly and estimated the four elements of the  
 454 impedance at five selected sites, L05, L02, L03, L01, and L04 (Yang et al., 2020, see Figure 7a  
 455 for their locations), where MT measurements were conducted. The estimations were made for  
 456 three periods, 100, 1,000 and 10,000 sec. Source combinations of  $\{a_1 \hat{\mathbf{S}}(45^\circ, 45^\circ), \hat{\mathbf{S}}(135^\circ, 45^\circ),$   
 457  $\hat{\mathbf{S}}(90^\circ, 135^\circ)\}$ , where  $a_1$  is  $10^{-0.5}$ , and  $\{\hat{\mathbf{S}}_{\zeta'}, \hat{\mathbf{S}}_{\eta'}, \hat{\mathbf{S}}_{\xi'}\}$  were used. As shown in Figure 7b, the F-  
 458 norm deviations of all five sites are significantly small, at the level between  $10^{-5}$  and  $10^{-3}$ .  
 459 However, the results changed dramatically when the 3-D anomaly was introduced. As shown in  
 460 Figure 7c, the F-norm deviations calculated at two sites (L04 and L05) near the edge of the  
 461 anomaly were several orders of magnitude larger than those at a site (L03) far from the  
 462 boundary. These large deviations exceeded the typical observation error level of 0.01.

463 The modeling results, together with those of the oceanic model, suggest that the  
 464 spherical MT impedances estimated from the three independent sources are non-unique when the  
 465 structure is laterally heterogeneous (See also Figure S8).



466 (a) (b) (c)

467 **Figure 7.** (a) A map showing the study region and site locations of the continental model. Green  
 468 crosses show the five selected sites (Yang et al., 2020). Green rectangle shows the location of the  
 469 3-D anomaly. (b) The F-norm deviations of the spherical impedances with source combinations  
 470 of  $\{a_1 \hat{\mathbf{S}}(45^\circ, 45^\circ), \hat{\mathbf{S}}(135^\circ, 45^\circ), \hat{\mathbf{S}}(90^\circ, 135^\circ)\}$  where  $a_1$  is  $10^{-0.5}$  and  $\{\hat{\mathbf{S}}_{\zeta'}, \hat{\mathbf{S}}_{\eta'}, \hat{\mathbf{S}}_{\xi'}\}$  at the five  
 471 selected sites in the continental model (b) without a 3-D anomaly, and (c) those with a 3-D  
 472 anomaly.

## 473 5 Impedance including the induction by the radial magnetic component

### 474 5.1 Tippers and impedance non-uniqueness

475 Thus far, we have observed that the impedance consisting of four elements, as estimated  
 476 in a spherical coordinate system, is not unique but rather depends on the source amplitude. This  
 477 non-uniqueness is more pronounced in areas near coastlines or boundaries of lateral  
 478 heterogeneity. Such lateral contrasts in electrical conductivity are known to cause anomalous  
 479 radial components of the induced magnetic field (e.g., Parkinson, 1959; Schmucker, 1970;  
 480 Kruglvakov & Kuvshinov, 2022). These observations strongly suggest that induction by the  
 481 radial magnetic component plays an important role in the non-uniqueness of the four elements of  
 482 the MT impedance calculated in a spherical coordinate system using Eq. (28).

483 To further investigate the relationship between the radial magnetic component and the  
 484 non-uniqueness of the impedance, we examined the behavior of tippers (geomagnetic transfer



485 functions). Tippers describe a linear relation between the tangential and radial magnetic  
486 components as:

$$487 \quad H_r = T_\theta H_\theta + T_\varphi H_\varphi + \delta\epsilon_{H_r}, \quad (29)$$

488 where  $T_\theta$  and  $T_\varphi$  are the  $\theta$ - and  $\varphi$ -components of the tipper, respectively, and  $\delta\epsilon_{H_r}$  is a residual  
489 term of linear fitting. To compare two tipper vectors, we used the L2-norm deviation, defined as:

$$490 \quad dT^{1-2} = \frac{\|\mathbf{T}^1 - \mathbf{T}^2\|_2}{\|\mathbf{T}^2\|_2}. \quad (30)$$

491 where the L2-norm of a tipper vector is given by:

$$492 \quad \|\mathbf{T}\|_2 = \left\{ |T_\theta|^2 + |T_\varphi|^2 \right\}^{1/2}. \quad (31)$$

493 We also defined the averaged L2-norm deviation of tippers over the entire study region as:

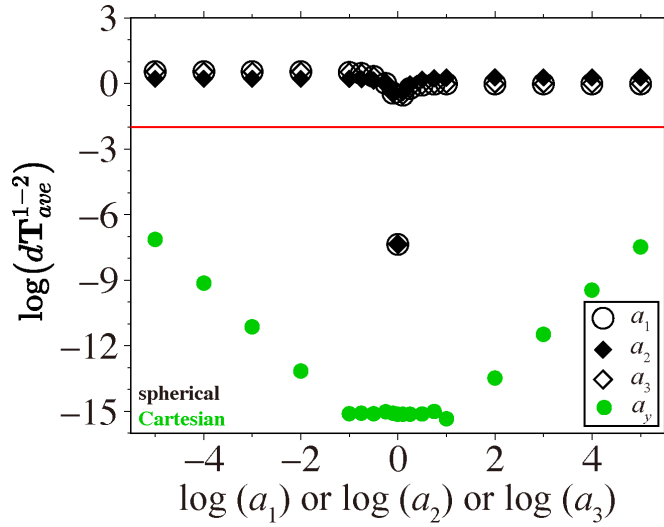
$$494 \quad dT_{avg}^{1-2} = \frac{1}{N} \sum_{n=1, N} \frac{\|\mathbf{T}_n^1 - \mathbf{T}_n^2\|_2}{\|\mathbf{T}_n^2\|_2}, \quad (32)$$

495 similar to the average F-norm deviation of the MT impedances given by Eq. (6). Superscripts 1  
496 and 2 denote the tippers for the two-source combinations of variable amplitude factors and those  
497 for a reference source combination  $\{\hat{\mathbf{S}}_{\zeta'}, \hat{\mathbf{S}}_{\eta'}, \hat{\mathbf{S}}_{\xi'}\}$ , respectively.

498 Kruglyakov and Kuvshinov (2022) modeled tippers in a spherical coordinate system with  
499 a plane-wave treatment by creating a source that does not produce a radial magnetic component  
500 at the Earth's surface. However, the radial component of the source magnetic field does not need  
501 to vanish at the Earth's surface as long as the condition for plane-wave approximation is satisfied  
502 for the primary field; that is, the induction wavenumber dominates the source wavenumber  
503 (Utada, 2018). This condition is satisfied in the present study, given the values of electrical  
504 conductivity and the period range used in the modeling calculations. Additionally, it is not  
505 feasible to select different sources to estimate the MT impedances and tippers from the field data.  
506 Therefore, we used external dipoles, the same sources as those used to estimate impedances in  
507 Section 4 (Figure 6), for the calculation of tippers on the spherical Earth.

508 Figure 8 shows the numerical modeling results for the continental model (see also Figure  
509 S9), presenting the averaged L2-norm deviations of the tippers. These deviations were calculated  
510 when  $a_1$  (represented by open black circles),  $a_2$  (represented by solid black diamonds), and  $a_3$   
511 (represented by open black diamonds) varied between  $10^{-5}$  and  $10^5$ . Overall, the average  
512 deviation of the tippers (Figure 8) closely resembles the behavior of the impedances (Figure 6).  
513 The deviations are approximately  $10^{-8}$  and  $10^{-7}$  when the amplitude factor is near unity, whereas  
514 they increase sharply when the amplitude factor deviates slightly from unity. The deviations are  
515 stable at high values, ranging between  $10^{-1}$  and 1 when the amplitude factors are smaller than  $10^{-2}$   
516 or larger than  $10^2$ . Figure 8 also illustrates the behavior of Cartesian tippers (represented by  
517 solid green circles). In this case, the amplitude of the E-W source was varied from  $10^{-5}$  to  $10^5$ ,  
518 while the amplitude of the N-S source was held constant at unity. The tippers were then  
519 evaluated and compared with those obtained when both source amplitudes were set to unity, to  
520 calculate the average deviations. The deviations of the Cartesian tippers are significantly smaller  
521 than those of the spherical tippers and remain stable at approximately  $10^{-15}$  or smaller than  $10^{-10}$ .

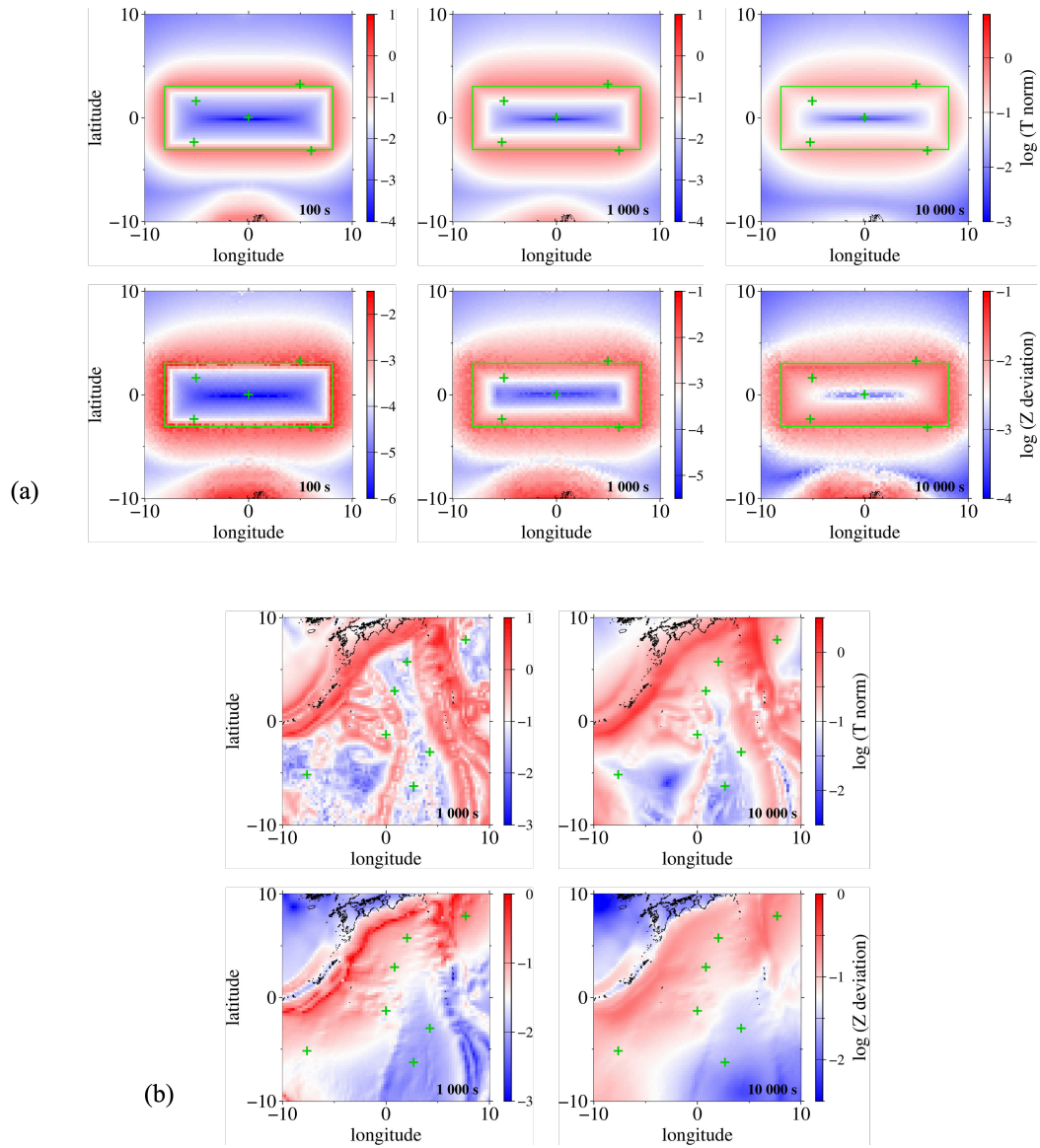
522 This result suggests that Cartesian tippers can be regarded as a unique EM response function,  
 523 unlike spherical tippers.



524

525 **Figure 8.** Dependence of  $dT_{avg}^{1-2}$  on  $\log(a_1)$ ,  $\log(a_2)$ , or  $\log(a_3)$  in a range when  $a_1$ ,  $a_2$ , or  $a_3$  is  
 526 between  $10^{-0.5}$  and  $10^{0.5}$  in the entire study region at a period of 10,000 sec. Open black circles  
 527 represent  $dZ_{avg}^{1-2}$  between tippers from source combination of  $\{a_1 \hat{\mathbf{S}}(45^\circ, 45^\circ), \hat{\mathbf{S}}(135^\circ, 45^\circ),$   
 528  $\hat{\mathbf{S}}(90^\circ, 135^\circ)\}$ ; and from  $\{\hat{\mathbf{S}}_{\zeta'}, \hat{\mathbf{S}}_{\eta'}, \hat{\mathbf{S}}_{\xi'}\}$ , solid black diamonds between those from source  
 529 combination of  $\{\hat{\mathbf{S}}(45^\circ, 45^\circ), a_2 \hat{\mathbf{S}}(135^\circ, 45^\circ), \hat{\mathbf{S}}(90^\circ, 135^\circ)\}$  and from  $\{\hat{\mathbf{S}}_{\zeta'}, \hat{\mathbf{S}}_{\eta'}, \hat{\mathbf{S}}_{\xi'}\}$ , and open  
 530 black diamonds between those from  $\{\hat{\mathbf{S}}(45^\circ, 45^\circ), \hat{\mathbf{S}}(135^\circ, 45^\circ), a_3 \hat{\mathbf{S}}(90^\circ, 135^\circ)\}$ , and  $\{\hat{\mathbf{S}}_{\zeta'}, \hat{\mathbf{S}}_{\eta'},$   
 531  $\hat{\mathbf{S}}_{\xi'}\}$ . Solid green circles represent deviations between 4-element Cartesian impedances (See  
 532 Appendix B). Model: the continental model with a 3-D anomaly in a rotated spherical coordinate  
 533 system and in a Cartesian coordinate system with the azimuthal equidistant projection (e.g.,  
 534 Snyder, 1987).

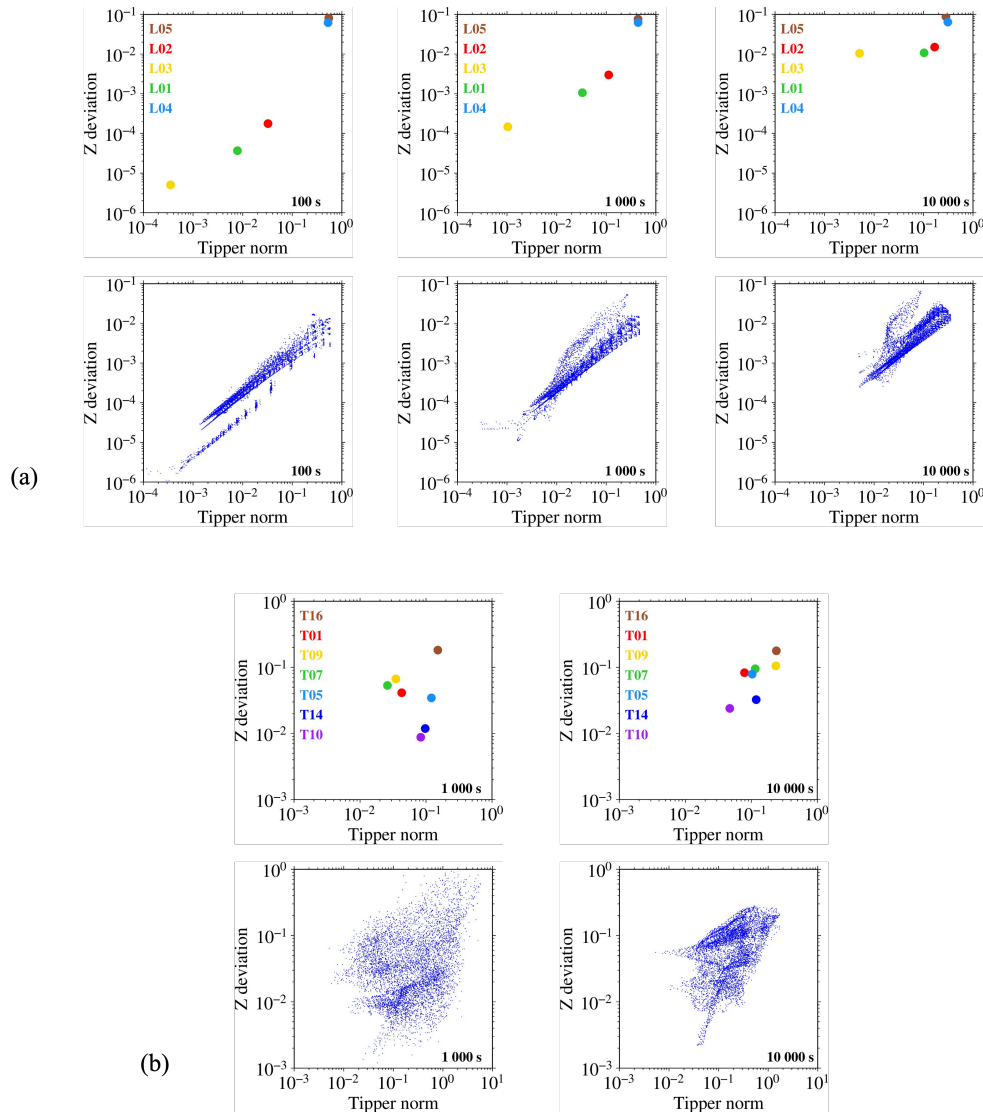
535 Figure 9a and 9b show maps of the L2-norm of tippers and the F-norm deviation of  
 536 impedances for the continental model with a high conductivity anomaly and for the oceanic  
 537 model, respectively. In these maps, tipper norms are obtained using a source combination of  
 538  $\{\hat{\mathbf{S}}_{\zeta'}, \hat{\mathbf{S}}_{\eta'}, \hat{\mathbf{S}}_{\xi'}\}$  and impedance deviations are obtained between the impedances for the source  
 539 combinations of  $\{a_1 \hat{\mathbf{S}}(45^\circ, 45^\circ), \hat{\mathbf{S}}(135^\circ, 45^\circ), \hat{\mathbf{S}}(90^\circ, 135^\circ)\}$ , where  $a_1$  is  $10^{-0.5}$ , and  $\{\hat{\mathbf{S}}_{\zeta'}, \hat{\mathbf{S}}_{\eta'},$   
 540  $\hat{\mathbf{S}}_{\xi'}\}$ . A strong correlation is observed between the two maps. Figures 10a and 10b display a  
 541 correlation plot between the impedance deviations and tipper norms for the continental and  
 542 oceanic models, respectively. Figure 10a demonstrates a clear positive correlation between the  
 543 impedance deviation and tipper norm for the continental model whereas Figure 10b indicates a  
 544 similar but weaker positive correlation for the oceanic model. The results from both numerical  
 545 experiments suggest that the impedance deviation due to the source amplitude effect tends to  
 546 increase with the tipper norm.



547

548 **Figure 9.** Top: Logarithm of tipper norms calculated with  $\{\hat{\mathbf{S}}_{\zeta'}, \hat{\mathbf{S}}_{\eta'}, \hat{\mathbf{S}}_{\xi'}\}$ . Bottom: Logarithm of  
 549 F-norm deviations between impedances calculated from source combinations of  $\{a_1 \hat{\mathbf{S}}(45^\circ, 45^\circ)$ ,

550  $\hat{\mathbf{S}}(135^\circ, 45^\circ), \hat{\mathbf{S}}(90^\circ, 135^\circ)\}$  when  $a_1$  is  $10^{-0.5}$  and  $\{\hat{\mathbf{S}}_{\zeta'}, \hat{\mathbf{S}}_{\eta'}, \hat{\mathbf{S}}_{\xi'}\}$ . (a) for the continental model  
 551 and (b) for the oceanic model, in a rotated spherical coordinate system.



552

553 **Figure 10.** Dependence of F-norm impedance deviation on tipper norm at selected sites (top) and  
 554 at all grid points at the surface of the Earth in the study region (bottom). Tippers are calculated  
 555 from  $\{\hat{\mathbf{S}}_{\zeta'}, \hat{\mathbf{S}}_{\eta'}, \hat{\mathbf{S}}_{\xi'}\}$ . F-norm impedance deviations are calculated between results from  
 556  $\{a_1 \hat{\mathbf{S}}(45^\circ, 45^\circ), \hat{\mathbf{S}}(135^\circ, 45^\circ), \hat{\mathbf{S}}(90^\circ, 135^\circ)\}$  where  $a_1$  is  $10^{-0.5}$  and  $\{\hat{\mathbf{S}}_{\zeta'}, \hat{\mathbf{S}}_{\eta'}, \hat{\mathbf{S}}_{\xi'}\}$ , (a) for the  
 557 continental model and (b) for the oceanic model, in a rotated spherical coordinate system.

558 5.2 6-element spherical impedance

559 The positive correlation between the impedance deviation and tipper norm obtained in the  
 560 previous section strongly suggests that the radial component of the magnetic field (both source  
 561 and induced) contributes to the non-uniqueness of the spherical impedance. Based on these  
 562 findings and a simple theoretical consideration of the impedance when the primary field includes

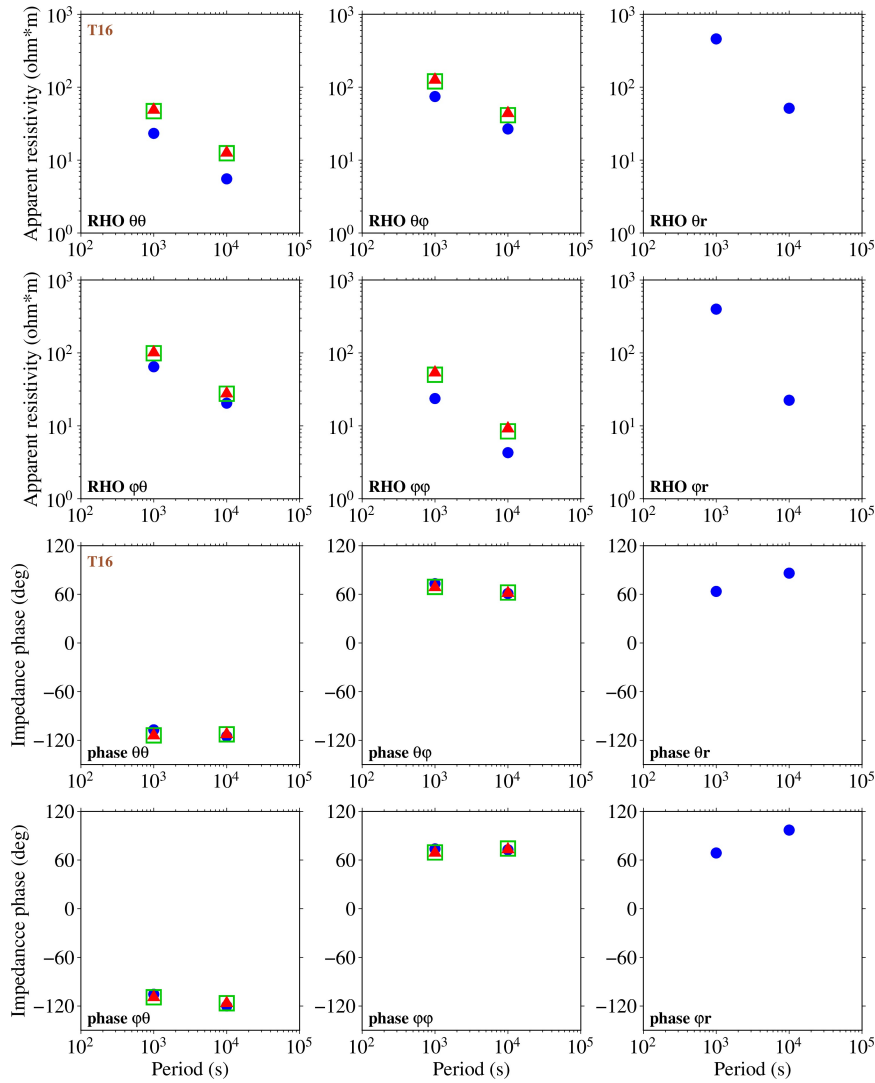
563 a vertical component (Appendix A), we introduced a new MT impedance in a spherical model  
 564 that accounts for induction by the radial magnetic component.

565 In general, the linear relation between three components of the electric and magnetic  
 566 fields in a conductive medium is expressed by a complex-valued  $3 \times 3$  impedance tensor. Since  
 567 the radial component of the electric field diminishes at the surface of the Earth, the new MT  
 568 impedance  $\mathbf{Z}^U$  becomes a complex-valued  $2 \times 3$  matrix. This impedance can be determined by  
 569 solving a linear equation relating the EM components from three independent sources:

$$570 \begin{pmatrix} E_{\theta}^1 & E_{\theta}^2 & E_{\theta}^3 \\ E_{\varphi}^1 & E_{\varphi}^2 & E_{\varphi}^3 \end{pmatrix} = \begin{pmatrix} Z_{\theta\theta}^U & Z_{\theta\varphi}^U & Z_{\theta r}^U \\ Z_{\varphi\theta}^U & Z_{\varphi\varphi}^U & Z_{\varphi r}^U \end{pmatrix} \begin{pmatrix} H_{\theta}^1 & H_{\theta}^2 & H_{\theta}^3 \\ H_{\varphi}^1 & H_{\varphi}^2 & H_{\varphi}^3 \\ H_r^1 & H_r^2 & H_r^3 \end{pmatrix}. \quad (33)$$

571 Hereafter, we refer to the new impedance with symbol  $U$  as the 6-element spherical impedance,  
 572 where the notation with superscript  $U$  distinguishes it from the spherical impedance consisting of  
 573 four elements (hereafter referred to as the 4-element impedance) calculated using Eq. (26) or  
 574 (28). Dmitriev and Berdichevsky (2002) proposed the 6-element impedance in a Cartesian model  
 575 and named it a generalized impedance. They introduced a method to calculate the impedance  
 576 using 3-D Cartesian forward modeling, although no calculation results have been reported thus  
 577 far.

578 Figure 11 presents the apparent resistivities and impedance phases at site T16 in the  
 579 oceanic model, which is the site nearest to the coastline. The results from the 4-element spherical  
 580 impedances for  $\{\hat{\mathbf{S}}_{\zeta'}, \hat{\mathbf{S}}_{\eta'}\}$  (represented by solid red triangles) or  $\{\hat{\mathbf{S}}_{\zeta'}, \hat{\mathbf{S}}_{\eta'}, \hat{\mathbf{S}}_{\xi'}\}$  (represented by  
 581 open green squares), as well as those from the 6-element spherical impedance for  $\{\hat{\mathbf{S}}_{\zeta'}, \hat{\mathbf{S}}_{\eta'}, \hat{\mathbf{S}}_{\xi'}\}$   
 582 (represented by solid blue circles) are shown. The results indicate that apparent resistivities  
 583 calculated from  $Z_{\theta r}^U$  and  $Z_{\varphi r}^U$  are of a similar order of magnitude to those estimated from the  
 584 other four elements.

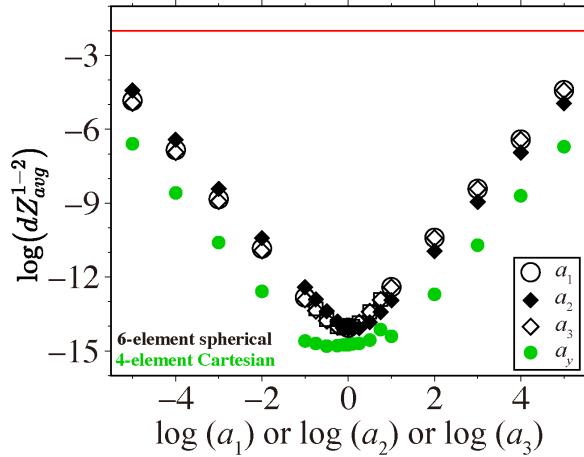


585

586 **Figure 11.** Period dependence of apparent resistivities and impedance phases at T16. Solid red  
 587 triangles: 4-element impedances from  $\{\hat{\mathbf{S}}_{\zeta'}, \hat{\mathbf{S}}_{\eta'}\}$ ; open green squares: 4-element impedances  
 588 from  $\{\hat{\mathbf{S}}_{\zeta'}, \hat{\mathbf{S}}_{\eta'}, \hat{\mathbf{S}}_{\xi'}\}$ ; solid blue circles: 6-element impedances from  $\{\hat{\mathbf{S}}_{\zeta'}, \hat{\mathbf{S}}_{\eta'}, \hat{\mathbf{S}}_{\xi'}\}$ . Model: the  
 589 oceanic model in a rotated spherical coordinate system.

590 The source amplitude dependence of the estimated impedances in the oceanic model was  
 591 further examined using the source combinations  $\{a_1 \hat{\mathbf{S}}(45^\circ, 45^\circ), \hat{\mathbf{S}}(135^\circ, 45^\circ), \hat{\mathbf{S}}(90^\circ, 135^\circ)\}$ ,  
 592  $\{\hat{\mathbf{S}}(45^\circ, 45^\circ), a_2 \hat{\mathbf{S}}(135^\circ, 45^\circ), \hat{\mathbf{S}}(90^\circ, 135^\circ)\}$  and  $\{\hat{\mathbf{S}}(45^\circ, 45^\circ), \hat{\mathbf{S}}(135^\circ, 45^\circ), a_3 \hat{\mathbf{S}}(90^\circ, 135^\circ)\}$ ,  
 593 which are the same source combinations used in Section 4 (Figure 6). The 6-element impedance  
 594 from a combination of the three basis sources was used as the reference. Figure 12 shows the  
 595 averaged F-norm deviations of the 6-element spherical impedances obtained when each value of  
 596 the amplitude factor  $a_1$  (represented by open black circles),  $a_2$  (represented by solid black  
 597 diamonds), or  $a_3$  (represented by open black diamonds) was varied from  $10^{-5}$  to  $10^5$ . The  
 598 deviations are on the order of  $10^{-14}$  when the amplitude factors are near unity and remain below  
 599  $10^{-5}$  across the entire range of amplitude factors examined, which can be considered as  
 600 sufficiently small compared with the target level of 0.01. Considering that the convergence

601 criterion in our numerical calculation was set to  $10^{-16}$ , deviations on the order of  $10^{-14}$  can be  
 602 attributed to the accumulated numerical errors. Therefore, the 6-element spherical impedance can  
 603 be regarded as essentially unique.



604

605 **Figure 12.** Dependence of  $dZ_{avg}^{1-2}$  on  $\log(a_1)$ ,  $\log(a_2)$ , or  $\log(a_3)$  in a range when  $a_1$ ,  $a_2$ , or  $a_3$  is  
 606 between  $10^{-5}$  and  $10^5$  in the entire study region at period of 10,000 sec. Open black circles  
 607 represent averaged deviations between 6-element impedances from source combinations  
 608  $\{a_1 \hat{\mathbf{S}}(45^\circ, 45^\circ), \hat{\mathbf{S}}(135^\circ, 45^\circ), \hat{\mathbf{S}}(90^\circ, 135^\circ)\}$ , and  $\{\hat{\mathbf{S}}_{\zeta'}, \hat{\mathbf{S}}_{\eta'}, \hat{\mathbf{S}}_{\xi'}\}$ , solid black diamonds between  
 609 those from  $\{\hat{\mathbf{S}}(45^\circ, 45^\circ), a_2 \hat{\mathbf{S}}(135^\circ, 45^\circ), \hat{\mathbf{S}}(90^\circ, 135^\circ)\}$  and  $\{\hat{\mathbf{S}}_{\zeta'}, \hat{\mathbf{S}}_{\eta'}, \hat{\mathbf{S}}_{\xi'}\}$ , and open black  
 610 diamonds between those from  $\{\hat{\mathbf{S}}(45^\circ, 45^\circ), \hat{\mathbf{S}}(135^\circ, 45^\circ), a_3 \hat{\mathbf{S}}(90^\circ, 135^\circ)\}$ , and  $\{\hat{\mathbf{S}}_{\zeta'}, \hat{\mathbf{S}}_{\eta'}, \hat{\mathbf{S}}_{\xi'}\}$ .  
 611 Solid green circles represent deviations between 4-element Cartesian impedances (See Appendix  
 612 B). Model: the oceanic model in a rotated spherical coordinate system and in a Cartesian  
 613 coordinate system with the azimuthal equidistant projection.

614 Results of similar numerical experiments in a Cartesian coordinate system are  
 615 represented by solid green circles in Figure 12 (See Appendix B for details). These results  
 616 demonstrate that the level of uniqueness of the 6-element spherical impedance is comparable to  
 617 that of the 4-element Cartesian impedance. We conclude that both the 4-element Cartesian  
 618 impedance and the 6-element spherical impedance are independent of the source amplitude and  
 619 can be employed as EM response functions.

## 620 6 Discussion

621 The 4- and 6-element spherical impedances are examined numerically in Sections 4 and  
 622 5, respectively. In Section 5, we found that tippers and 4-element impedances are related. Here  
 623 we demonstrate that tipper plays an important role in causing the non-uniqueness of the 4-  
 624 element impedance. The 6-element impedance  $\mathbf{Z}^U$  in Eq. (33) can be substituted into the 4-  
 625 element impedance  $\mathbf{Z}$  in Eq. (26) using the tipper components  $T_\theta$  and  $T_\phi$  in Eq. (29). Substituting  
 626 Eq. (29) into Eq. (33), while ignoring the residual term  $\delta\epsilon_{H_r}$ , we can approximately express the  
 627 4-element impedance in terms of the 6-element impedance and tippers as

$$628 \quad Z_{\theta\theta} \approx Z_{\theta\theta}^U + Z_{\theta r}^U T_\theta, \quad (34)$$

$$629 \quad Z_{\theta\phi} \approx Z_{\theta\phi}^U + Z_{\theta r}^U T_\phi, \quad (35)$$

630 
$$Z_{\varphi\theta} \approx Z_{\varphi\theta}^U + Z_{\varphi r}^U T_{\theta}, \quad (36)$$

631 and

632 
$$Z_{\varphi\varphi} \approx Z_{\varphi\varphi}^U + Z_{\varphi r}^U T_{\varphi}. \quad (37)$$

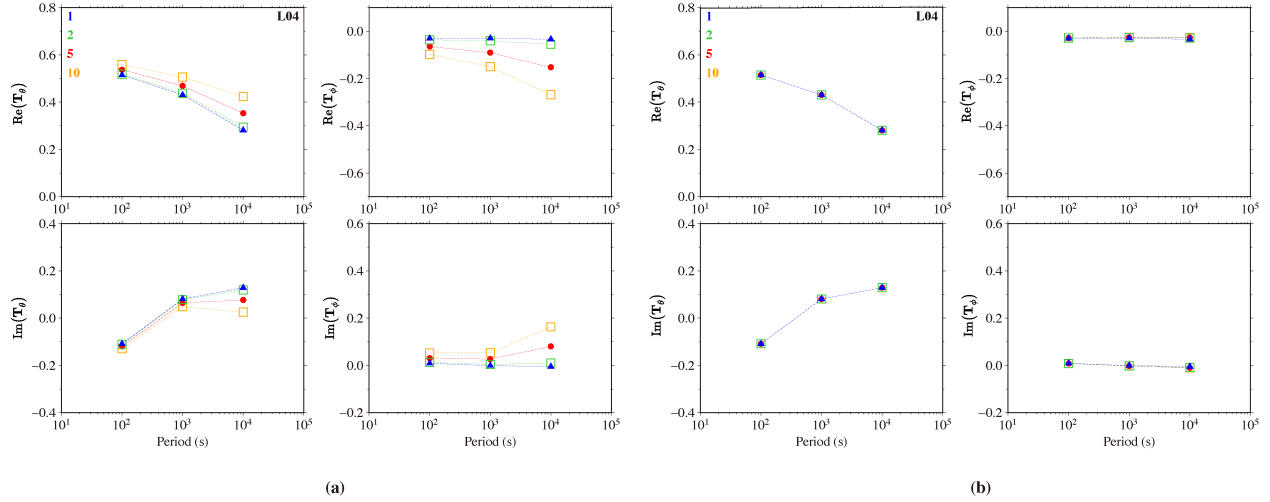
633 Dmitriev and Berdichevsky (2002) derive a similar relationship in a Cartesian coordinate system.

634 This relationship can account for certain properties of the 4-element spherical impedance, particularly its non-uniqueness, because the 6-element spherical impedance is shown to be  
 635 unique, while the tippers are not. More precisely, the 4-element spherical impedance is not a  
 636 unique response of the Earth's conductivity structure but exhibits considerable source amplitude  
 637 dependence unless the Earth's structure is nearly 1-D (laterally uniform), where the tippers are  
 638 negligible so that the second terms on the right-hand side of Eqs. (34)–(37) are also negligible.  
 639

640 As an application of this relationship, we consider seasonal variations in tippers and MT  
 641 impedances, which have been documented in different land regions across a wide range of  
 642 periods (e.g., Kappler et al., 2010; Brändlein et al., 2012; Araya et al., 2013; Ernst et al., 2020,  
 643 2022). Ernst et al. (2020, 2022) reported that seasonal variations in tippers were more significant  
 644 than those in 4-element impedances, attributing this to variations of the external radial (vertical)  
 645 magnetic component. Based on this observation and considering the role of tippers in connecting  
 646 the 6-element to the 4-element spherical impedance (Eqs. (34)–(37)), it would be valuable to  
 647 examine the behavior of tippers for different amplitudes of the radial component of the source  
 648 fields in spherical models. In this study, we used a continental model with one 3-D anomaly  
 649 (Figure 7) because this model exhibits a simple and clear pattern with large tippers only near the  
 650 boundaries of the lateral conductivity contrasts (Figure 9).

651 We examined tippers with the source combination  $\{\hat{\mathbf{S}}_{\zeta'}, \hat{\mathbf{S}}_{\eta'}, a_{\xi'} \hat{\mathbf{S}}_{\xi'}\}$  and  $\{\hat{\mathbf{S}}_{\zeta'}, a_{\eta'} \hat{\mathbf{S}}_{\eta'},$   
 652  $\hat{\mathbf{S}}_{\xi'}\}$ , where the amplitude factors  $a_{\xi'}$  and  $a_{\eta'}$  were set to 1, 2, 5, or 10. This test allows us to  
 653 separately analyze the influence of the radial and tangential components of the external magnetic  
 654 fields on the tippers. We selected site L04, located near the northern edge of the conductivity  
 655 contrast, where significant amplitudes of the tippers were expected (Figure 9a). The calculated  
 656 tipper amplitude showed a tendency to increase with  $a_{\xi'}$  (Figure 13a). However, changes in  $T_{\varphi}$  is  
 657 more pronounced than those in  $T_{\theta}$ . This tendency is opposite to the observation by Ernst et al.  
 658 (2020), where variations in  $T_{\theta}$  were larger than those in  $T_{\varphi}$ . In contrast, variations in the tippers  
 659 when  $a_{\eta'}$  was varied (Figure 13b) were significantly smaller than those observed for variations  
 660 in  $a_{\xi'}$  (Figure 13a). Based on these results, we focused on the case of varying  $a_{\xi'}$ , which  
 661 corresponds to the influence of changes in the radial magnetic component of the external field.

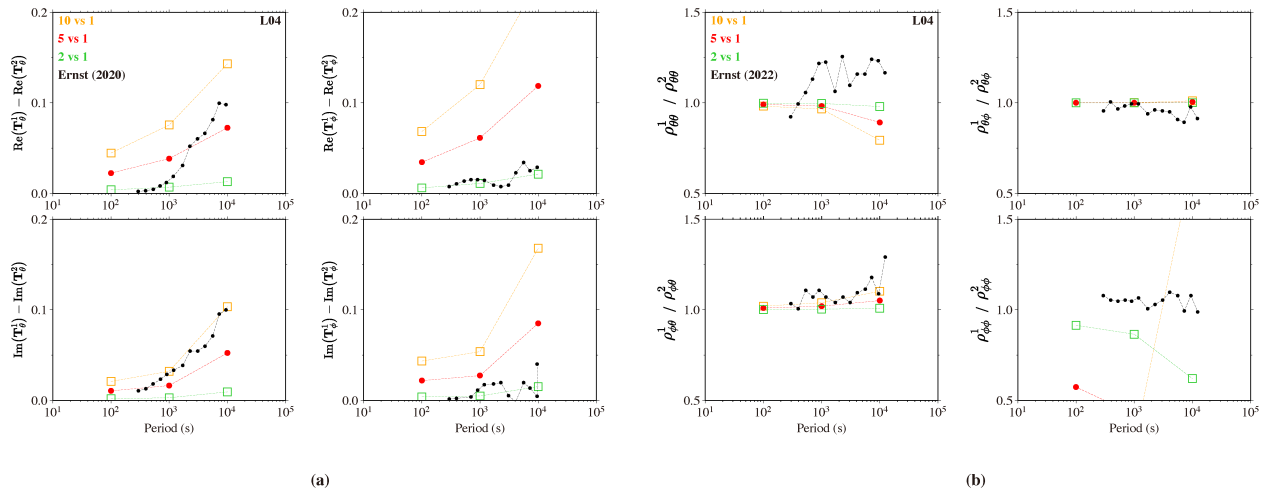




662

663 **Figure 13.** Dependence of tipper on period at site L04 when amplitudes (a)  $a_{\xi'}$  in  $\{\hat{\mathbf{S}}_{\zeta'}, \hat{\mathbf{S}}_{\eta'},$   
 664  $a_{\xi'} \hat{\mathbf{S}}_{\xi'}\}$  or (b)  $a_{\eta'}$  in  $\{\hat{\mathbf{S}}_{\zeta'}, a_{\eta'} \hat{\mathbf{S}}_{\eta'}, \hat{\mathbf{S}}_{\xi'}\}$  has different values. Blue solid triangles, green open  
 665 squares, red solid circles, and orange open squares indicate results when the source amplitude  
 666  $a_{\xi'}$  or  $a_{\eta'}$  is 1, 2, 5 and 10, respectively. Model: the continental model with a 3-D anomaly in a  
 667 rotated spherical coordinate system.

668 Figure 14a shows the difference in tippers observed by Ernst et al. (2020), who calculated  
 669 the absolute seasonal differences between tippers estimated from the magnetic field data in  
 670 summer and winter (represented by black solid circles). Additionally, the absolute differences in  
 671 the real and imaginary parts between two tippers, which were calculated in this study with  
 672 various  $a_{\xi'}$  and those with  $a_{\xi'} = 1$  at L04, are shown in Figure 14a. We found that the seasonal  
 673 changes in the real and imaginary parts of  $T_{\theta}$  reported by Ernst et al. (2020) can be roughly  
 674 explained by a change in the amplitude of the source radial magnetic component between 1 (at  
 675 shorter periods) and 9 (at longer periods) and those of  $T_{\varphi}$  can be explained by a smaller change,  
 676 approximately 1. Although fitting the continental model results to the observations of Ernst et al.  
 677 (2020) is not the main aim of this study, these findings suggest that the magnitude of seasonal  
 678 variations in tippers can be explained by varying the amplitude of the external radial magnetic  
 679 component using only degree-one (spatially uniform) sources.



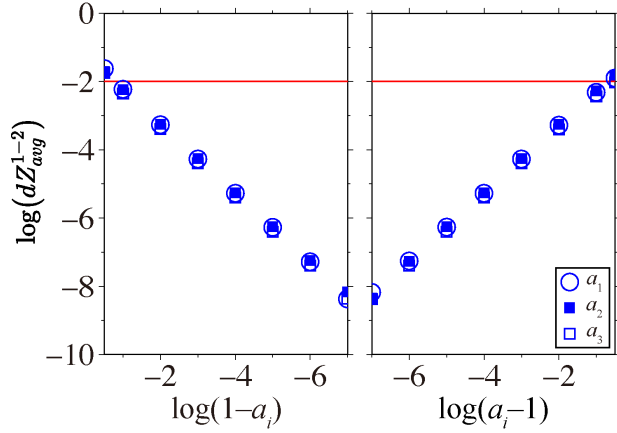
680

681 **Figure 14.** Period dependence of (a) absolute differences in tipper norm and (b) apparent  
 682 resistivity at L04 for different values of the source amplitude ( $a_{\xi'}=1, 2, 5$  or  $10$ ). Model: the  
 683 continental model with a 3-D anomaly in a rotated spherical coordinate system.

684 We further examined the apparent resistivity differences at site L04 for varying  $a_{\xi'}$   
 685 values and compared them to those obtained from observed data by Ernst et al. (2022) as shown  
 686 in Figure 14b. Differences of approximately 0.01 in  $\rho_{a_{\varphi\theta}}$  and 0.1 in  $\rho_{a_{\theta\varphi}}$  at a period of 10,000  
 687 sec at L04 could be attributed to a case where  $a_{\xi'} \approx 10$ . A more detailed discussion of the  
 688 amplitude differences between the sources requires the use of a more realistic model of electrical  
 689 conductivity below the study area in Europe. We also suggest that examining six elements of the  
 690 impedance, rather than four, would better capture time-dependent changes in the Earth's  
 691 electrical conductivity. This is because the 6-element impedance is independent of the source  
 692 amplitude, so far as only external dipoles are considered.

693 To gain deeper insights into the uniqueness and non-uniqueness of the 6- and 4-element  
 694 spherical impedances, we analyzed cases where one of the amplitude factors ( $a_{1a\_1a1}$ ,  $a_{2a\_2a2}$ ,  
 695 or  $a_{3a\_3a3}$ ) of the three independent sources was varied (Figure 12). For the 6-element  
 696 impedance, the average deviation remained nearly constant at a negligibly small value ( $\sim 10^{-14}$ )  
 697 when the amplitude factor ranged between  $10^{-1}$  and  $10^1$  (Figure 12). In contrast, we observe a  
 698 gradually increasing trend in the average deviation when the amplitude factor is smaller than  $10^{-1}$   
 699 or larger than  $10^1$  (Figure 12). This occurs because the amplitude of one of the three orthogonal  
 700 sources is significantly smaller or greater than that of the other two, accumulating rounding  
 701 errors in solving Eq. (33) for the six impedance elements. Nevertheless, acceptable solutions  
 702 were still obtained within a wide amplitude range of  $10^{-5}$  to  $10^5$  (Figure 12). These results  
 703 indicate that estimating unique values of the 6-element impedances is stable and feasible for  
 704 most combinations of the three external dipole sources over a broad amplitude range.

705 In contrast, in the case of 4-element spherical impedance, we observed a sudden and  
 706 significant increase in the F-norm deviations when the amplitude factor of one of the three  
 707 independent sources slightly deviated from unity (Figure 6). Figure 15 shows the detailed  
 708 behavior of the deviations for the ranges of  $a_1$ ,  $a_2$ , and  $a_3$  corresponding to the hatched interval  
 709 in Figure 6. The deviations continued to increase for amplitudes decreasing from unity to  $10^{-1}$   
 710 or increasing from unity to  $10^1$ , and then remained nearly stable at values between 0.01 and 1 for  
 711 further decreasing or increasing amplitudes (Figure 6). This behavior suggests that unique  
 712 estimation of the 4-element spherical impedances may be possible, but only under limited  
 713 condition where the given sources to be decomposed into three orthogonal sources with nearly  
 714 equal amplitudes. However, the minimum deviation of the 4-element impedance is notably larger  
 715 than that of the 6-element impedance.



716

717 **Figure 15.** Dependence of  $dZ_{avg}^{1-2}$  on  $\log(1-a_i)$  or  $\log(a_i-1)$  ( $i=1, 2$  or  $3$ ) in a range between  $-7$   
 718 and  $-0.5$  (hatched area in Figure 6) in the whole study region at period of 10,000 sec. Symbols  
 719 are the same with Figure 6. Model: the oceanic model in a rotated spherical coordinate system.

720 Note that the residual terms in Eq. (28) of the overdetermined problem to estimate the 4-  
 721 element impedance are significant. Here, we define the averaged residual across the entire study  
 722 region for the external source  $k$  as:

$$723 \quad d\epsilon_{\mathbf{E}}^k = \frac{1}{N} \sum_{n=1,N} \frac{\|\delta\epsilon_{\mathbf{E}}^k\|_2}{\|\mathbf{E}^k\|_2}, \quad (38)$$

724 where subscript  $n$  represents a calculation cell in the study region, and  $N$  is the total number of  
 725 cells for the oceanic model or the continental model. For a source combination of  $\{\hat{\mathbf{S}}_{\zeta'}, \hat{\mathbf{S}}_{\eta'}, \hat{\mathbf{S}}_{\xi'}\}$ ,  
 726 the average residuals for the three sources are listed in Table 1 for two periods. We noticed  
 727 relatively large residuals for  $\hat{\mathbf{S}}_{\xi'}$ , indicating the significant influence of ignoring the induction by  
 728 the radial magnetic components when calculating the 4-element impedance. The effects of  
 729 induction by the radial magnetic component are incorporated into the four elements through the  
 730 linear relationships in Eqs. (34)–(37). As a result, the impedance relation expressed using the 4-  
 731 element impedance is inaccurate, particularly for  $\hat{\mathbf{S}}_{\xi'}$  which generates a source field oriented  
 732 nearly in the radial direction within the study region (Table 1). This explains why the deviation  
 733 of the 4-element impedance cannot be as small as that of the 6-element impedance, even when  
 734 three basis sources are given.

735 **Table 1**

736 *Averaged residuals  $d\epsilon_{\mathbf{E}}^k$  when calculating 4-element impedances from the source combination of*  
 737  *$\{\hat{\mathbf{S}}_{\zeta'}, \hat{\mathbf{S}}_{\eta'}, \hat{\mathbf{S}}_{\xi'}\}$ . Model: oceanic model in the rotated spherical coordinate system.*

Source	T = 1,000 s	10,000 s
$\hat{\mathbf{S}}_{\zeta'}$	0.0112	0.0080
$\hat{\mathbf{S}}_{\eta'}$	0.0121	0.0090
$\hat{\mathbf{S}}_{\xi'}$	0.5837	0.6174

738 The source effect discussed thus far is observed only in the 4-element spherical  
739 impedance, which we call the “source amplitude effect.” In general, any source combination can  
740 be decomposed into three basis sources with specific amplitude factors. The source amplitude  
741 effect in 4-element spherical impedance arises when the amplitude factors of decomposed three  
742 orthogonal sources are unequal. However, questions remain, such as how significant the non-  
743 uniqueness of the 4-element spherical impedance is and whether estimating the 6-element  
744 spherical impedance is necessary in practice. Further investigation is required to address these  
745 questions. Once the validity of using the 6-element impedance is established, both modeling and  
746 inversion of MT observational data should be conducted in a spherical coordinate system rather  
747 than in a Cartesian coordinate system.

748 Another type of source effect is known to exist, which affects both the 4- and 6-element  
749 spherical impedances. We refer to this as the “source harmonic degree effect”, caused by sources  
750 with different harmonic degrees. This type of source effect similarly manifests in the Cartesian  
751 MT impedance as the source wavenumber effect, also known as the source dimension effect (see  
752 Appendix A). The large impedance residual for the source  $\hat{S}_{\xi'}$ , which increases with period  
753 (Table 1), can be partially attributed to this effect. While addressing how to properly account for  
754 this effect at higher harmonic degrees in a spherical coordinate system is an important problem,  
755 it is beyond the scope of this study.

## 756 **7 Conclusions**

757 In this study, we conducted systematic MT modeling in a spherical coordinate system,  
758 using laterally heterogeneous oceanic and continental models to examine the effects of source  
759 polarization and amplitude on the MT impedance. Our results revealed that the 4-element  
760 spherical impedance, estimated from two independent sources, is non-unique and exhibits  
761 considerable dependence on source polarization and amplitude, unless the Earth’s structure is  
762 nearly 1-D. When three independent sources are applied, the 4-element spherical impedance no  
763 longer exhibits a source polarization effect; however, source amplitude dependence persists. We  
764 observed that the non-uniqueness in the 4-element spherical impedance is positively correlated  
765 with the tipper norm. Based on this observation and a simple theoretical consideration (Appendix  
766 A), we introduced a new impedance model consisting of six elements, which incorporates  
767 induction by the radial magnetic components. Our findings demonstrated that the 6-element  
768 spherical impedance can be uniquely estimated, independent of the amplitude of three  
769 independent dipole sources. However, tippers remain non-unique even when three independent  
770 sources are applied. Furthermore, we established that the 6-element impedance can be related to  
771 the 4-element impedance through tippers. This relationship provides potential explanations for  
772 observed seasonal variations in tippers and 4-element impedances, which may result from  
773 variations in the amplitudes of the radial components of the external magnetic field. The 6-  
774 element impedance is a unique function only of the Earth’s conductivity structure and frequency,  
775 and it is independent of the source amplitude. Therefore, the 6-element impedance is expected to  
776 serve as a more reliable EM response function for inverting the field data.

777 **Appendix A**

778 Impedance relation including the source wavenumber for a uniform half-space

779 Here, we address the solution of the EM induction equation in a Cartesian coordinate  
 780 system with the origin at the Earth's surface. We consider the behavior of the primary EM field  
 781 within a uniform half-space (conductivity  $\sigma$ ) in response to the incidence of an external magnetic  
 782 field polarized in the  $x$ - $z$  plane with wavenumber  $\nu$  and angular frequency  $\omega$ , where  $z$  points  
 783 vertically downward. At the surface ( $z = 0$ ) and within the Earth, two components of the  
 784 magnetic field ( $H_x$  and  $H_z$ ) and one component of the electric field ( $E_y$ ) can be expressed as  
 785 (e.g., Utada, 2018):

786 
$$H_x(x, \omega) = \frac{i\nu\gamma}{\mu_0} \epsilon_1(\nu, \omega) e^{-\nu z} e^{i\nu x}, \quad (\text{A1})$$

787 
$$H_z(x, \omega) = \frac{i\nu^2}{\mu_0} \epsilon_1(\nu, \omega) e^{-\nu z} e^{i\nu x}, \quad (\text{A2})$$

788 and

789 
$$E_y(x, \omega) = -\omega\nu\epsilon_1(\nu, \omega) e^{-\nu z} e^{i\nu x}, \quad (\text{A3})$$

790 where  $\epsilon_1$  is a coefficient to be determined by applying a boundary condition at the surface,  $\mu_0$  is  
 791 the magnetic permeability, and  $\gamma = \sqrt{\nu^2 + i\omega\sigma\mu_0}$ . The impedance relation for  $E_y$  can be  
 792 obtained from Ampere's law as:

793 
$$\begin{aligned} E_y(x, \omega) &= \left(\frac{1}{\sigma} \frac{\partial}{\partial z}\right) H_x(\nu, \omega) - \left(\frac{1}{\sigma} \frac{\partial}{\partial x}\right) H_z(\nu, \omega) \\ &= Z_{yx}^U(\nu, \omega) \cdot H_x(\nu, \omega) + Z_{yz}^U(\nu, \omega) \cdot H_z(\nu, \omega). \end{aligned} \quad (\text{A4})$$

795 Using (A1)–(A4), we derive the expressions for the  $yx$ - and  $yz$ -elements of the MT  
 796 impedance as follows:

797 
$$Z_{yx}^U(\nu, \omega) = \frac{1}{\sigma} \frac{\partial H_x(\nu, \omega)}{\partial z} \Big/ H_x(\nu, \omega) = -\frac{\gamma}{\sigma} \quad (\text{A5})$$

798 and

799 
$$Z_{yz}^U(\nu, \omega) = -\frac{1}{\sigma} \frac{\partial H_z(\nu, \omega)}{\partial x} \Big/ H_z(\nu, \omega) = \frac{-i\nu}{\sigma}. \quad (\text{A6})$$

800 If the combination of  $\omega$  and  $\sigma$  satisfies the condition for the plane-wave approximation  
 801 ( $\nu^2 \ll |i\omega\sigma\mu_0|$ ),  $Z_{yz}^U$  vanishes and  $Z_{yx}^U$  approaches the well-known expression of the MT  
 802 impedance first presented by Cagniard (1953). Note that  $Z_{yz}^U$  is purely imaginary because it is  
 803 caused by eddy currents.

804 Price (1962) derived an MT impedance element  $Z_{yx}^P$  directly from Eqs. (A1) and (A3):

805 
$$Z_{yx}^P(\nu, \omega) = \frac{E_y(x, \omega)}{H_x(\nu, \omega)} = \frac{i\omega\mu_0}{\gamma}. \quad (\text{A7})$$

806 This expression is mathematically correct but not physically consistent, as it combines two  
807 induced electric fields arising from different mechanisms.

## 808 **Appendix B**

### 809 MT modeling in a Cartesian coordinate system

810 The source effects in a Cartesian coordinate system were examined by forward modeling  
811 using the ModEM code, which employed the finite difference method (Egbert & Kelbert, 2012).  
812 In this code, two uniform external source fields polarized in the N-S and E-W directions are  
813 assigned at the top boundary (1629 km in altitude) of the model domain.

814 We adopted a nearly identical grid spacing for both the spherical and Cartesian modeling  
815 studies, as well as for both the oceanic and continental models, to facilitate the comparison. For  
816 numerical modeling in a Cartesian coordinate system, the grid design of the two shallowest  
817 layers is the same as that in the spherical modeling, except for grids near the seafloor. To  
818 accurately estimate the MT impedance at the seafloor in the oceanic model, where there is a  
819 significant contrast in electrical conductivity between the layers above and below, 13 additional  
820 grids with denser spacing were employed near the seafloor. Such treatment was necessary  
821 because the ModEM code interpolates the magnetic field components from values at grids above  
822 and below the seafloor, whereas the spherical code extrapolates values from two grids below the  
823 seafloor (Tada et al., 2012). We confirmed that Cartesian and spherical solutions give consistent  
824 estimates of the MT impedance for a 1-D case (See Figure S3). The vertical grid spacing near the  
825 seafloor is also confirmed to be sufficiently fine for a 3-D model (See Figure S3).

826 The horizontal size of the Cartesian modeling domain was set to  $10\,007.538\,6\text{ km} \times 10$   
827  $007.538\,6\text{ km}$  ( $\sim 40^\circ \times 40^\circ$ ). The horizontal grid spacing was set to  $27.7\,987\text{ km}$  ( $\sim 0.25^\circ$ ) in the  
828 study region and gradually widened to  $111.1\,949\text{ km}$  ( $\sim 1^\circ$ ),  $222.3\,898\text{ km}$  ( $\sim 2^\circ$ ), and  $555.9\,745$   
829  $\text{km}$  ( $\sim 5^\circ$ ), depending on the distance from the study region. In total, there were 84 grid points in  
830 the  $z$ -direction and 176 grid points in both the  $x$ - and  $y$ -directions.

831 Here, we present numerical results from three experiments to demonstrate that the  
832 Cartesian impedance is independent of both source polarization and amplitude, using the oceanic  
833 model. Note that the calculated impedance elements were converted to those in the original  
834 coordinate system for consistency with an actual field measurement. The position vector at any  
835 location is defined by  $\mathbf{r} = (x, y, z)^t$ , where  $x$ ,  $y$ , and  $z$  denote the geographical northward,  
836 eastward, and downward directions, respectively. The superscript  $t$  denotes the transpose. The  
837 azimuthal equidistant projection (e.g., Snyder, 1987) is employed for the map projection.

838 Let a plane-wave source with arbitrary polarization and amplitude in the Cartesian  
839 coordinate system be denoted as  $\mathbf{S}(\gamma_S)$ , where the azimuth  $\gamma_S$  represents the angle from the  $x$ -  
840 direction (Figure B1). The source  $\mathbf{S}(\gamma_S)$  can be decomposed into two basis sources as:

$$841 \quad \mathbf{S}(\gamma_S) = a_x \hat{\mathbf{S}}_x + a_y \hat{\mathbf{S}}_y, \quad (\text{B1})$$

842 where  $a_x$  and  $a_y$  are amplitude factors. By normalizing  $\mathbf{S}$ , we can derive a plane-wave source of  
843 unit amplitude with arbitrary polarization as:

$$844 \quad \hat{\mathbf{S}}(\gamma_S) = \hat{a}_x \hat{\mathbf{S}}_x + \hat{a}_y \hat{\mathbf{S}}_y, \quad (\text{B2})$$

845 where

$$846 \quad \hat{a}_x = \frac{a_x}{|\mathbf{S}(\gamma_S)|} = \cos(\gamma_S) \quad (\text{B3})$$

847 and

$$848 \quad \hat{a}_y = \frac{a_y}{|\mathbf{S}(\gamma_S)|} = \sin(\gamma_S). \quad (\text{B4})$$

849 Let the external magnetic field due to an arbitrary source  $\mathbf{S}(\gamma_S)$  in a Cartesian coordinate  
850 system be denoted as  $\mathbf{H}_{ext}(\mathbf{r}, \omega, \mathbf{S})$ . Using Eq. (B1) and the linearity of the EM field, we derive:

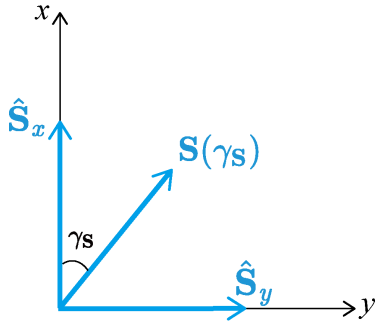
$$851 \quad \mathbf{H}_{ext}(\mathbf{r}, \omega, \mathbf{S}) = a_x \mathbf{H}_{ext}(\mathbf{r}, \omega, \hat{\mathbf{S}}_x) + a_y \mathbf{H}_{ext}(\mathbf{r}, \omega, \hat{\mathbf{S}}_y). \quad (\text{B5})$$

852 The solution of Maxwell's equations,  $\mathbf{E}(\mathbf{r}, \omega, \mathbf{S})$  and  $\mathbf{H}(\mathbf{r}, \omega, \mathbf{S})$ , for an arbitrary source  
853  $\mathbf{S}(\gamma_S)$  in a Cartesian coordinate system can then be obtained as linear combinations of the solutions  
854 for two basis sources:

$$855 \quad \mathbf{E}(\mathbf{r}, \omega, \mathbf{S}) = a_x \mathbf{E}(\mathbf{r}, \omega, \hat{\mathbf{S}}_x) + a_y \mathbf{E}(\mathbf{r}, \omega, \hat{\mathbf{S}}_y), \quad (\text{B6})$$

856 and

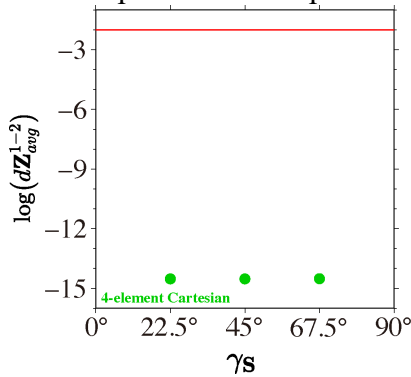
$$857 \quad \mathbf{H}(\mathbf{r}, \omega, \mathbf{S}) = a_x \mathbf{H}(\mathbf{r}, \omega, \hat{\mathbf{S}}_x) + a_y \mathbf{H}(\mathbf{r}, \omega, \hat{\mathbf{S}}_y). \quad (\text{B7})$$



858

859 **Figure B1.** External sources in the Cartesian coordinate system.  $\mathbf{S}$  is a source of arbitrary  
860 polarization (azimuth  $\gamma_S$ ) and amplitude.

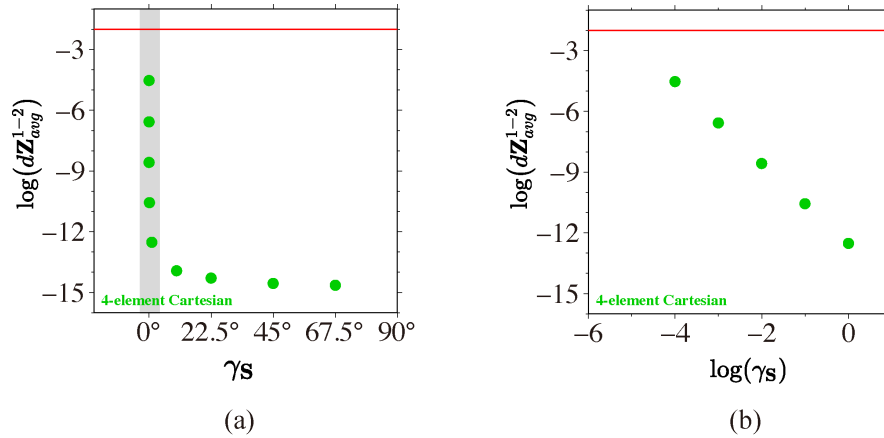
861 Here we have tested three cases. In Case 1, the polarizations of two orthogonal sources  
862 were changed by the same angle  $\gamma_S$  to calculate  $\mathbf{E}(\mathbf{r}, \omega, \mathbf{S})$  and  $\mathbf{H}(\mathbf{r}, \omega, \mathbf{S})$ . The external source  
863 combination in this case was  $\{\hat{\mathbf{S}}(\gamma_S), \hat{\mathbf{S}}(\gamma_S + 90^\circ)\}$ , where  $\gamma_S = 22.5^\circ, 45^\circ,$  and  $67.6^\circ$ . The resulting  
864 impedances were compared with those for the source combination  $\{\hat{\mathbf{S}}(0^\circ), \hat{\mathbf{S}}(90^\circ)\}$  to calculate  
865 the averaged deviation across the entire study region. As shown in Figure B2, the averaged  
866 deviation is consistently between  $10^{-14}$  and  $10^{-15}$ , suggesting that the Cartesian impedance is unique  
867 and independent of the polarizations of the two sources.



868

869 **Figure B2.** Dependence of  $dZ_{avg}^{1-2}$  on  $\gamma_S$  when  $\gamma_S=22.5^\circ$ ,  $45^\circ$ , and  $67.5^\circ$  in the entire study region  
 870 at a period of 10,000 sec. Model: Cartesian oceanic model with azimuthal equidistant projection  
 871 method.

872 In Case 2, the polarization of only one external source was changed, resulting in two  
 873 sources that were not orthogonal. The external source combination is denoted as  $\{\hat{\mathbf{S}}_x, \hat{\mathbf{S}}(\gamma_S)\}$ ,  
 874 which can also be expressed as  $\{\hat{\mathbf{S}}_x, \cos(\gamma_S)\hat{\mathbf{S}}_y + \sin(\gamma_S)\hat{\mathbf{S}}_z\}$  by definition. The results shown in  
 875 Figure B3 suggest that the Cartesian impedance is unique unless  $\gamma_S$  is nearly equal to zero, i.e.,  
 876 unless the two sources are almost parallel.  
 877



878 (a) (b)

879 **Figure B3.** Dependence of  $dZ_{avg}^{1-2}$  on (a)  $\gamma_S$  when  $\gamma_S$  is between  $10^{-50}$  and  $67.5^\circ$  and (b)  $\log(\gamma_S)$   
 880 (corresponding to the shaded zone in (a)) in the entire study region at period of 10,000 sec.  
 881 Model: Cartesian oceanic model with azimuthal equidistant projection method.

882 In Case 3, the amplitude of one of two orthogonal sources was chosen to be variable. The  
 883 source combination is denoted as  $\{\hat{\mathbf{S}}_x, a_y \hat{\mathbf{S}}_y\}$ , where the amplitude factor  $a_y$  varies between  $10^{-5}$   
 884 and  $10^5$ . The results, shown in Figure 12, indicate that the Cartesian impedance is independent of  
 885 the source amplitude.

886 We summarize the results of the above three cases that the Cartesian impedances calculated  
 887 from a combination of EM fields generated from two independent sources are unique and  
 888 independent of the source amplitude and polarization. The source polarization effect in Case 2 can  
 889 be regarded as a source amplitude effect when the amplitude of one source is very small. However,  
 890 in Case 3, we confirmed the absence of the source amplitude effect even when the amplitude is  
 891 either very small or very large. Therefore Case 3 provides a more general examination of this  
 892 phenomenon.

### 893 Acknowledgments

894 We thank Makoto UYESHIMA for providing an original 3-D spherical modeling code. We  
 895 thank Ömer Faruk BODUR and Kiyoshi BABA for their comments. We thank Alexander



896 GRAYVER, Anna KELBERT and two associate editors for their valuable comments and  
897 suggestions.

898 This study was partially supported by Geological Joint Fund of National Natural Science  
899 Foundation of China (Key Fund Project, under Grant No. U2344203), National Natural Science  
900 Foundation of China (under Grant No. 42474105, 42074079), JSPS KAKENHI (grant  
901 #21H01186), Interdisciplinary Project in Ocean Research of Tongji University and the  
902 Fundamental Research Funds for the Central Universities, Independent Project of the State Key  
903 Laboratory of Marine Geology at Tongji University (under Grant No. MGZ202403), Major  
904 Project of China National Petroleum Corporation (under Grant No. 2023ZZ05-05), and Jiangsu  
905 Province Carbon Peak Carbon Neutral Technology Innovation Project in China (under Grant  
906 No.BE2022034-3).

907 **Open Research**

908 The dataset used in the figures in this study can be accessed on Zenodo (Wan & Utada, 2024).  
909

910 **References**

- 911 Amante, C., & Eakins, B. W. (2009). ETOPO1 Global Relief Model converted to PanMap layer  
912 format. NOAA-National Geophysical Data Center, PANGAEA,  
913 doi:10.1594/PANGAEA.769615
- 914 Araya, J., Ritter, O., & Brändlein, D. (2013). Long-term variations of magnetotelluric transfer  
915 functions in northern Chile. In 25. Schmucker-Weidelt-Kolloquium für Elektromagnetische  
916 Tiefenforschung (pp. 124–129).
- 917 Baba, K., Utada, H., Goto, T. N., Kasaya, T., Shimizu, H., & Tada, N. (2010). Electrical  
918 conductivity imaging of the Philippine Sea upper mantle using seafloor magnetotelluric data.  
919 *Physics of the Earth and Planetary Interiors*, 183(1–2), 44–62. doi:10.1016/j.pepi.2010.09.010
- 920 Banks, R. J. (1969). Geomagnetic variations and the electrical conductivity of the upper mantle.  
921 *Geophysical Journal International*, 17(5), 457–487. doi:10.1111/j.1365-246X.1969.tb00252.x
- 922 Berdichevsky, M. N. (1999). Marginal notes on Magnetotellurics. *Surveys in Geophysics*, 20,  
923 341–375. doi:10.1023/A:1006645715819
- 924 Berdichevsky, M. N. & Dmitriev, V.I. (1997). On deterministic nature of magnetotelluric  
925 impedance, *Acta Geophysica Polonica XLV*(3), 227–236
- 926 Brändlein, D., Lühr, H., & Ritter, O. (2012). Direct penetration of the interplanetary electric field  
927 to low geomagnetic latitudes and its effect on magnetotelluric sounding. *Journal of Geophysical*  
928 *Research: Space Physics*, 117(A11). doi:10.1029/2012JA018008
- 929 Cagniard, L. (1953). Basic theory of the magneto-telluric method of geophysical prospecting.  
930 *Geophysics*, 18(3), 605–635. doi:10.1190/1.1437915
- 931 Chave, A. D., & Jones, A. G. (Eds.). (2012). *The magnetotelluric method: Theory and practice*.  
932 Cambridge University Press. doi:10.1017/CBO9781139020138

- 933 Dmitriev, V. I. & Berdichevsky, M. N. (2002). A generalized Impedance Model. *Izvestiya,*  
934 *Physics of the Solid Earth*, 38(10), 897-903.
- 935 Egbert, G. D., & Kelbert, A. (2012). Computational recipes for electromagnetic inverse  
936 problems. *Geophysical Journal International*, 189(1), 251–267. doi:10.1111/j.1365-  
937 246X.2011.05347.x
- 938 Ernst, T., Nowożyński, K., & Józwiak, W. (2020). The reduction of source effect for reliable  
939 estimation of geomagnetic transfer functions. *Geophysical Journal International*, 221(1), 415–  
940 430. doi:10.1093/gji/ggaa017
- 941 Ernst, T., Nowożyński, K., & Józwiak, W. (2022). Source effect impact on the magnetotelluric  
942 transfer functions. *Annals of Geophysics*, 65(1), GM104–GM104. doi:10.4401/ag-8751
- 943 Fujita, S., Fujii, I., Endo, A., & Tominaga, H. (2018). Numerical modeling of spatial profiles of  
944 geomagnetically induced electric field intensity in and around Japan. *Tech Rep Kakioka Magn*  
945 *Observ*, 15, 35–50.
- 946 Garcia, X., Chave, A. D. & Jones, A. G. (1997). Robust processing of magnetotelluric data from  
947 the auroral zone. *Journal of geomagnetism and geoelectricity*, 49 (11-12), 1451-1468. doi:  
948 10.5636/jgg.49.1451
- 949 Garcia, X., & Jones, A. G. (2000). Advances in aspects of the application of magnetotellurics for  
950 mineral exploration. In *SEG Technical Program Expanded Abstracts 2000* (pp. 1115–1118).  
951 Society of Exploration Geophysicists. doi:10.1190/1.1815583
- 952 Grayver, A. V., van Driel, M., & Kuvshinov, A. V. (2019). Three-dimensional magnetotelluric  
953 modelling in spherical Earth. *Geophysical Journal International*, 217(1), 532–557.  
954 doi:10.1093/gji/ggz030

- 955 Grayver, A. V., Munch, F. D., Kuvshinov, A. V., Khan, A., Sabaka, T. J., & Tøffner - Clausen,  
956 L. (2017). Joint inversion of satellite - detected tidal and magnetospheric signals constrains  
957 electrical conductivity and water content of the upper mantle and transition zone. *Geophysical*  
958 *research letters*, 44(12), 6074–6081. doi:10.1002/2017GL073446
- 959 Guzavina, M., Grayver, A., & Kuvshinov, A. (2019). Probing upper mantle electrical  
960 conductivity with daily magnetic variations using global-to-local transfer functions. *Geophysical*  
961 *Journal International*, 219(3), 2125–2147. doi:10.1093/gji/ggz412
- 962 Han, Q., & Hu, X. (2023). Three-dimensional Magnetotelluric Modeling in Spherical and  
963 Cartesian Coordinate Systems: a Comparative Study. *Earth and Planetary Physics*, 7, 0–0.  
964 doi:10.26464/epp2023048
- 965 Han, Q., Hu, X., & Peng, R. (2020). Spherical magnetotelluric modeling based on non-uniform  
966 source. *Chinese Journal of Geophysics*, 63(8), 3154–3166. doi:10.6038/cjg2020N0207
- 967 Jiang, W., Duan, J., Doublier, M., Clark, A., Schofield, A., Brodie, R. C., & Goodwin, J. (2022).  
968 Application of multiscale magnetotelluric data to mineral exploration: an example from the east  
969 Tennant region, Northern Australia. *Geophysical Journal International*, 229(3), 1628–1645.  
970 doi:10.1093/gji/ggac029
- 971 Kappler, K. N., Morrison, H. F., & Egbert, G. D. (2010). Long - term monitoring of ULF  
972 electromagnetic fields at Parkfield, California. *Journal of Geophysical Research: Solid Earth*,  
973 115(B4). doi:10.1029/2009JB006421
- 974 Kruglyakov, M., & Kuvshinov, A. (2022). Modelling tippers on a sphere. *Geophysical Journal*  
975 *International*, 231(2), 737–748. doi:10.1093/gji/ggac199

- 976 Kuvshinov, A., & Semenov, A. (2012). Global 3-D imaging of mantle electrical conductivity  
977 based on inversion of observatory C-responses—I. An approach and its verification. *Geophysical*  
978 *Journal International*, 189(3), 1335–1352. doi:10.1111/j.1365-246X.2011.05349.x
- 979 Laske, G., & Masters, G. (1997). A Global Digital Map of Sediment Thickness. *EOS*  
980 *Transactions American Geophysical Union*, 78, F483.
- 981 Livelybrooks, D. W., Mareschal, M., Blais, E., & Smith, J. T. (1996). Magnetotelluric  
982 delineation of the Trillabelle massive sulfide body in Sudbury, Ontario. *Geophysics*, 61(4), 971–  
983 986. doi:10.1190/1.1444046
- 984 Luo, W., Wang, X., Wang, K., Zhang, G., & Li, D. (2019). Three-dimensional forward modeling  
985 of the magnetotelluric method in spherical coordinates. *Chinese Journal of Geophysics*, 62(10),  
986 3885–3897. doi:10.6038/cjg2019M0439
- 987 Mackie, R. L., Smith, J. T., & Madden, T. R. (1994). Three - dimensional electromagnetic  
988 modeling using finite difference equations: The magnetotelluric example. *Radio Science*, 29(4),  
989 923–935. doi:10.1029/94RS00326
- 990 Mackie, R. L., Madden, T. R., & Wannamaker, P. E. (1993). Three-dimensional magnetotelluric  
991 modeling using difference equations; theory and comparisons to integral equation solutions.  
992 *Geophysics*, 58(2), 215–226. doi:10.1190/1.1443407
- 993 Matsuno, T., Suetsugu, D., Baba, K., Tada, N., Shimizu, H., Shiobara, H., et al. (2017). Mantle  
994 transition zone beneath a normal seafloor in the northwestern Pacific: Electrical conductivity,  
995 seismic thickness, and water content. *Earth and Planetary Science Letters*, 462, 189–198.  
996 doi:10.1016/j.epsl.2016.12.045

- 997 Newman, G. A., & Alumbaugh, D. L. (2000). Three-dimensional magnetotelluric inversion  
998 using non-linear conjugate gradients. *Geophysical journal international*, 140(2), 410–424.  
999 doi:10.1046/j.1365-246x.2000.00007.x
- 1000 Parkinson, W. D. (1959). Directions of rapid geomagnetic fluctuations. *Geophysical Journal*  
1001 *International*, 2(1), 1–14. doi:10.1111/j.1365-246X.1959.tb05776.x
- 1002 Price, A. T. (1962). The theory of magnetotelluric methods when the source field is considered.  
1003 *Journal of Geophysical Research*, 67(5), 1907–1918. doi:10.1029/JZ067i005p01907
- 1004 Rosell, O., Martí, A., Marcuello, À., Ledo, J., Queralt, P., Roca, E., & Campanyà, J. (2011).  
1005 Deep electrical resistivity structure of the northern Gibraltar Arc (western Mediterranean):  
1006 Evidence of lithospheric slab break - off. *Terra Nova*, 23(3), 179–186. doi:10.1111/j.1365-  
1007 3121.2011.00996.x
- 1008 Schmucker, U. (1970). An introduction to induction anomalies. *Journal of Geomagnetism and*  
1009 *Geoelectricity*, 22(1-2), 9–33. doi:10.5636/jgg.22.9
- 1010 Schmucker, U. (1987). Substitute conductors for electromagnetic response estimates. *Pure and*  
1011 *applied geophysics*, 125, 341-367. doi: 10.1007/BF00874501
- 1012 Schmucker, U. (1999a). A spherical harmonic analysis of solar daily variations in the years  
1013 1964–1965: response estimates and source fields for global induction—I. Methods. *Geophysical*  
1014 *Journal International*, 136(2), 439–454. doi:10.1046/j.1365-246X.1999.00742.x
- 1015 Schmucker, U. (1999b). A spherical harmonic analysis of solar daily variations in the years  
1016 1964–1965: response estimates and source fields for global induction—II. Results. *Geophysical*  
1017 *Journal International*, 136(2), 455–476. doi:10.1046/j.1365-246X.1999.00743.x

- 1018 Shimizu, H., Koyama, T., Baba, K., & Utada, H. (2010). Revised 1-D mantle electrical  
1019 conductivity structure beneath the north Pacific. *Geophysical Journal International*, 180(3),  
1020 1030–1048. doi:10.1111/j.1365-246X.2009.04466.x
- 1021 Shimizu, H., Yoneda, A., Baba, K., Utada, H., & Palshin, N. A. (2011). Sq effect on the  
1022 electromagnetic response functions in the period range between 104 and 105 s. *Geophysical*  
1023 *Journal International*, 186(1), 193–206. doi:10.1111/j.1365-246X.2011.05036.x
- 1024 Simpson, F., & Bahr, K. (2005). *Practical magnetotellurics*. Cambridge University Press.  
1025 doi:10.1017/CBO9780511614095
- 1026 Siripunvaraporn, W., Egbert, G., & Uyeshima, M. (2005). Interpretation of two-dimensional  
1027 magnetotelluric profile data with three-dimensional inversion: synthetic examples. *Geophysical*  
1028 *journal international*, 160(3), 804–814. doi:10.1111/j.1365-246X.2005.02527.x
- 1029 Snyder, J. P. (1987). *Map projections--A working manual* (Vol. 1395). US Government Printing  
1030 Office. doi:10.3133/pp1395
- 1031 Srivastava, S. P. (1966). Theory of the magnetotelluric method for a spherical conductor.  
1032 *Geophysical Journal International*, 11(4), 373–387. doi:10.1111/j.1365-246X.1966.tb03090.x
- 1033 Stanley, W. D., Boehl, J. E., Bostick, F. X., & Smith, H. W. (1977). Geothermal significance of  
1034 magnetotelluric sounding in the eastern Snake River Plain - Yellowstone region. *Journal of*  
1035 *Geophysical Research*, 82(17), 2501–2514. doi:10.1029/JB082i017p02501
- 1036 Strangway, D. W., Swift, C. M., & Holmer, R. C. (1973). The application of audio-frequency  
1037 magnetotellurics (AMT) to mineral exploration. *Geophysics*, 38(6), 1159–1175.  
1038 doi:10.1190/1.1440402

- 1039 Tada, N., Baba, K., Siripunvaraporn, W., Uyeshima, M., & Utada, H. (2012). Approximate  
1040 treatment of seafloor topographic effects in three-dimensional marine magnetotelluric inversion.  
1041 *Earth, planets and space*, 64, 1005–1021. doi:10.5047/eps.2012.04.005
- 1042 Tada, N., Baba, K., & Utada, H. (2014). Three - dimensional inversion of seafloor  
1043 magnetotelluric data collected in the Philippine Sea and the western margin of the northwest  
1044 Pacific Ocean. *Geochemistry, Geophysics, Geosystems*, 15(7), 2895–2917.  
1045 doi:10.1002/2014GC005421
- 1046 Tada, N., Tarits, P., Baba, K., Utada, H., Kasaya, T., & Suetsugu, D. (2016). Electromagnetic  
1047 evidence for volatile - rich upwelling beneath the society hotspot, French Polynesia.  
1048 *Geophysical Research Letters*, 43(23), 12021–12026. doi:10.1002/2016GL071331
- 1049 Utada, H. (2018). Plane-wave and flat Earth approximations in natural-source electromagnetic  
1050 induction studies. *Bull Earthq Res Inst Univ Tokyo*, 93, 1–14, doi:10.15083/0000051814
- 1051 Uyeshima, M., & Schultz, A. (2000). Geoelectromagnetic induction in a heterogeneous sphere: a  
1052 new three-dimensional forward solver using a conservative staggered-grid finite difference  
1053 method. *Geophysical Journal International*, 140(3), 636–650. doi:10.1046/j.1365-  
1054 246X.2000.00051.x
- 1055 Wan, X., & Utada, H. (2024). Dataset of modeling results. [Data set]. Zenodo.  
1056 <https://doi.org/10.5281/zenodo.10725054>
- 1057 Wannamaker, P. E., Hohmann, G. W., & Ward, S. H. (1984). Magnetotelluric responses of three-  
1058 dimensional bodies in layered earths. *Geophysics*, 49(9), 1517–1533. doi:10.1190/1.1441777
- 1059 Yang, W., Jin, S., Zhang, L., Qu, C., Hu, X., Wei, W., et al. (2020). The three-dimensional  
1060 resistivity structures of the lithosphere beneath the Qinghai-Tibet Plateau. *Chinese Journal of*  
1061 *Geophysics*, 63(3), 817–827. doi:10.6038/cjg2020N0197



1062 Zhang, H., Egbert, G. D., & Huang, Q. (2023). Constraints on MTZ water content from joint  
1063 inversion of diurnal variations and magnetospheric signals. *Geophysical Research Letters*,  
1064 50(10), e2023GL102765. doi:10.1029/2023GL102765

1065 Zhang, H., Huang, Q., Zhao, G., Guo, Z., & Chen, Y. J. (2016). Three-dimensional conductivity  
1066 model of crust and uppermost mantle at the northern Trans North China Orogen: Evidence for a  
1067 mantle source of Datong volcanoes. *Earth and Planetary Science Letters*, 453, 182–192.  
1068 doi:10.1016/j.epsl.2016.08.025